ERDC/GSL TR-19-9

Geotechnical and Structures Laboratory

US Army Corps of Engineers®
Engineer Research and Development Center

ERDC
ENGINEER RESEARCH & DEVELOPMENT CENTER

Introducing Additional Energy Dissipation Mechanisms in Steel Fiber Reinforcement for Ultra-High Performance Concrete

Dylan A. Scott, Robert D. Moser, Zackery B. McClelland, Sarah L. Williams, Brett A. Williams, Wendy R. Long, Brian H. Green, Kirk E. Walker, Christopher N. Downey, and Alexander J. Tillotson

March 2019

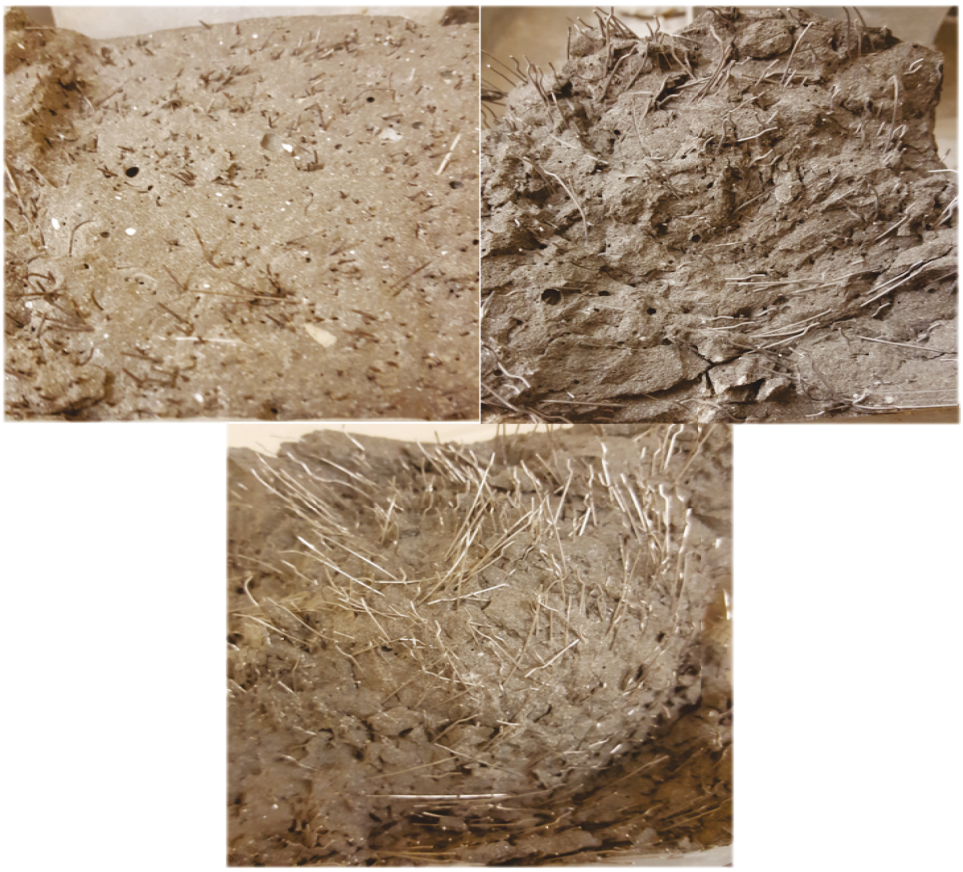

The U.S. Army Engineer Research and Development Center (ERDC) solves the nation's toughest engineering and environmental challenges. ERDC develops innovative solutions in civil and military engineering, geospatial sciences, water resources, and environmental sciences for the Army, the Department of Defense, civilian agencies, and our nation's public good. Find out more at www.erdc.usace.army.mil.

To search for other technical reports published by ERDC, visit the ERDC online library at http://acwc.sdp.sirsi.net/client/default.

ERDC/GSL TR-19-9
March 2019

Introducing Additional Energy Dissipation Mechanisms in Steel Fiber Reinforcement for Ultra-High Performance Concrete

Dylan A. Scott, Robert D. Moser, Zackery B. McClelland, Sarah L. Williams, Brett A. Williams, Wendy R. Long, Brian H. Green, Kirk E. Walker, Christopher N. Downey, and Alexander J. Tillotson

Geotechnical and Structural Laboratory
U.S. Army Engineer Research and Development Center
3909 Halls Ferry Road
Vicksburg, MS 39180-6199

Final report

Prepared for U.S. Army Corps of Engineers
Washington, DC 20314-1000

Under Project F7CJL4, "Stress-activated phase transformations and twinning for improved energy dissipation in composites"

Abstract

By adding annealed plain carbon steel fibers and stainless steel fibers into Ultra-High Performance Concrete (UHPC), researchers have increased UHPC's toughness through optimized thermal processing and alloy selection of steel fiber reinforcements. Currently, steel fiber reinforcements used in UHPCs are extremely brittle and have limited energy dissipation mainly through debonding due to matrix crumbling with some pullout. Implementing optimized heat treatments and selecting proper alternative alloys can drastically improve the post-yield carrying capacity of UHPCs for static and dynamic applications through plastic deformations, phase transformations, and fiber pullout. By using a phase transformable stainless steel, the ultimate flexural strength increased from 32.0 MPa to 42.5 MPa (33 percent) and decreased the post-impact or residual projectile velocity measurements an average of 31.5 m/s for 2.54-cm- and 5.08-cm-thick dynamic impact panels.

Contents

Abstract ii

Figures and Tables v

Preface vii

Unit Conversion Factors viii

1 Introduction 1

1.1 Background 1

1.1.1 Energy dissipation mechanisms of steel fibers 3

1.1.2 Phase transformation and stress activated plasticity 7

1.2 Research scope 8

2 UHPC Materials and Thermal Processing 10

2.1 UHPC materials 10

2.1.1 Cor-Tuf baseline UHPC 10

2.1.2 Steel fiber types 11

2.2 Thermal processing 12

2.3 Thermally processed materials 13

3 Experimental Methods 14

3.1 Quasi-static mechanical properties 14

3.1.1 Steel fiber tensile testing 14

3.1.2 Unconfined compressive strength 14

3.1.3 Flexural response 14

3.2 Dynamic penetration using fragment-simulating projectiles 15

3.3 Vibrating specimen magnetometer 16

4 Experimental Results and Discussion 18

4.1 Steel fiber tensile properties 18

4.2 Quasi-static results 19

4.3 Dynamic penetration results 23

4.3.1 2.54-cm-thick panels 23

4.3.2 5.18-cm-thick panels 25

4.3.3 6.35-cm-thick panels 28

4.4 Phase transformation verification 30

5 Future Work 33

5.1 Meta-stable steels: TRIP and TWIP 33

5.2 Manufacturability 34

6 Conclusions 35

References 36

Appendix A: BEKAERT Steel Fiber Data Sheets.....40

Appendix B: Dynamic Impact Pictures.....42

Report Documentation Page

Figures and Tables

Figures

Figure 1. Posttest flexural response beam (101.6 mm x 101.6 mm) showing intact carbon steel fibers. 2
Figure 2. ASTM 1609 flexural response from Scott et al. (2015). 4
Figure 3. Typical fiber pullout behavior for smooth and deformed fibers (Naaman and Najm 1991) 6
Figure 4. Theoretical optimal fiber tensile strength plot. 8
Figure 5. Bekaert Dramix 3D 55/30 BG fibers (Williams et al. 2009, Roth et al. 2010). 12
Figure 6. Thermal processing of CS fibers. 13
Figure 7. ASTM C 1609 for 101.6- x 101.6- x 457.2-mm flexural response beam. 15
Figure 8. Dynamic penetration test set-up (FSP – TL, Full test set-up – TR, Impact velocity chronographs – BL, Concrete panel with witness panel and residual velocity chronographs – BR). 16
Figure 9. Load versus elongation to failure for each fiber type. **Note 0.55-mm diameter for CS and AC; 0.38-mm diameter for SS and AS. 19
Figure 10. Flexural load versus center-line displacement 21
Figure 11. Post-test flexural response beams (101.6 mm x 101.6 mm) (AC - top left, CS - top right, SS - bottom) 22
Figure 12. Post-impact projectile for the SS 5.08-cm panel shot #6. 24
Figure 13. Graphical representation of average residual velocities (m/s) for 2.54-cm and 5.08-cm-thick panels. 27
Figure 14. Exit face spall for 6.35-cm panels (CS Shot #08 -TL, SS Shot #18 -TR, AC Shot #26 -B). 29
Figure 15. Magnetization saturation for posttest SS fiber samples. 31
Figure B16. Carbon steel dynamic impact 1-in. thickness. 42
Figure B17. Stainless steel dynamic impact 1-in. thickness. 43
Figure B18. Annealed carbon steel dynamic impact 1-in. thickness. 44
Figure B19. Carbon steel dynamic impact 2-in. thickness. 45
Figure B20. Stainless steel dynamic impact 2-in. thickness. 46
Figure B21. Annealed carbon steel dynamic impact 2-in. thickness. 47
Figure B22. Carbon steel dynamic impact 2.5-in. thickness. 48
Figure B23. Stainless steel dynamic impact 2.5-in. thickness 49
Figure B24. Annealed carbon steel dynamic impact 2.5-in. thickness. 50

Tables

Table 1. ASTM E1479-16 analysis of steel fiber reinforcement 11
Table 2. Quasi-static testing results. 20

Table 3. Dynamic impact results for 2.54-cm-thick panels. 25
Table 4. Dynamic impact results for 5.08-cm-thick panels. 26
Table 5. Dynamic impact results for 6.35-cm-thick panels. 29

Preface

This study was conducted for the ERDC Military Engineering Basic Research Program under Project F7CJL4, "Stress-activated phase transformations and twinning for improved energy dissipation in composites." The technical monitor was Dr. Robert D. Moser.

The work was performed by the Concrete and Materials Branch (GMC) of the Engineering Systems and Materials Division (GM), U.S. Army Engineer Research and Development Center, Geotechnical and Structures Laboratory (ERDC-GSL). At the time of publication, Mr. Christopher M. Moore was Chief, CEERD-GMC; Mr. Jeffrey G. Averett was Acting Chief, CEERD-GM; and Ms. Pamela G. Kinnebrew, CEERD-GZT, was the Technical Director for Military Engineering. The Deputy Director of ERDC-GSL was Mr. Charles W. Ertle II, and the Director was Mr. Bartley P. Durst.

COL Ivan P. Beckman was the Commander of ERDC, and Dr. David W. Pittman was the Director.

Unit Conversion Factors

Multiply	By	To Obtain
cubic feet	0.02831685	cubic meters
cubic inches	1.6387064 E-05	cubic meters
cubic yards	0.7645549	cubic meters
degrees Fahrenheit	(F-32)/1.8	degrees Celsius
feet	0.3048	meters
foot-pounds force	1.355818	joules
gallons (U.S. liquid)	3.785412 E-03	cubic meters
inches	0.0254	meters
pounds (force)	4.448222	newtons
pounds (force) per square inch	6.894757	kilopascals
pounds (mass)	0.45359237	kilograms
pounds (mass) per cubic foot	16.01846	kilograms per cubic meter
pounds (mass) per square foot	4.882428	kilograms per square meter
pounds (mass) per square yard	0.542492	kilograms per square meter
square feet	0.09290304	square meters
square inches	6.4516 E-04	square meters
tons (2,000 pounds, mass)	907.1847	kilograms
yards	0.9144	meters

1 Introduction

Advances in the science of concrete and materials have led to the development of some relatively new classes of concrete, specifically ultra-high performance concrete (UHPC; Graybeal 2011). UHPC is a concrete that exhibits exceptional strength and durability properties, making it well-suited for civil and military applications. UHPC is a class of concrete that typically exhibits compressive strengths in excess of 140 MPa and high durability due to negligible interconnected porosity. High toughness is achieved with the addition of fiber reinforcement.

1.1 Background

UHPC formulations generally consist of a high cementitious content incorporating oil-well or low-heat portland cement, siliceous or aluminous fine aggregates, crushed quartz or some other micrometer-sized powder, silica fume, water, high-range water-reducing admixtures to control rheology, and other components that vary by manufacturer. With the high compressive strengths of UHPC comes brittle behavior similar to that of a ceramic material. To overcome this brittle behavior, steel fiber reinforcement is commonly used at volume fractions ranging from 1-4 percent. The addition of steel fiber reinforcement aids in delocalizing micro- and macro-scale cracking and leads to improvements in tensile properties and minimized spallation during failure.

Various UHPC formulations exist with the majority being developed by manufacturers. The matrices, i.e., the portions of the UHPC excluding the fiber reinforcement, are generally similar in composition and basic mechanical properties, such as compressive and tensile strengths. The variations observed in UHPC failure morphology when subjected to extreme loading events are largely related to the steel fiber reinforcement, including its strength, length, and diameter, as well as any deformations present that provide mechanical interlock with the matrix.

Rivera-Soto et al. (2016) state “One of the inherent limitations of typical metallic reinforcement results from the way it is produced.” Steel fiber diameter typically ranges from 0.2 mm to 0.5 mm (Graybeal 2006). The heavy, cold drawing required during production of small-diameter fibers results in extremely high tensile strengths and low ductility of 1-5 percent

making the fibers a relatively brittle material. Current fiber reinforcements have limited energy dissipation controlled mainly by matrix fracturing with no plastic deformation and little pullout. Often times a steel fiber's deformation mechanism (i.e. hooked-end, undulation, or twisting) is never engaged due to crumbling of the UHPC matrices around the fiber. Banthia and Trottier (1994) show quantifiable evidence that with higher-strength concrete matrices, premature fiber pullout failure occurs due to brittle matrix splitting. Figure 1 shows a posttest flexural beam reinforced with as-manufactured hooked-end steel fiber that was subjected to a 4-point flexural test. Most of the fibers and their hooked-end deformation mechanisms are still intact. Some of the fibers are straight, suggesting some pullout has occurred, but there is no evidence of plastic deformation. In order to improve toughness in composite materials, an increased ductility of fiber reinforcement is necessary as well as modifying fiber yield strength such that plasticity occurs as fibers are engaged (Rivera-Soto et al. 2016). Through optimized heat treatments and proper alloy selection, new energy deformation mechanisms could be introduced, thus improving toughness.

Figure 1. Posttest flexural response beam (101.6 mm x 101.6 mm) showing intact carbon steel fibers.

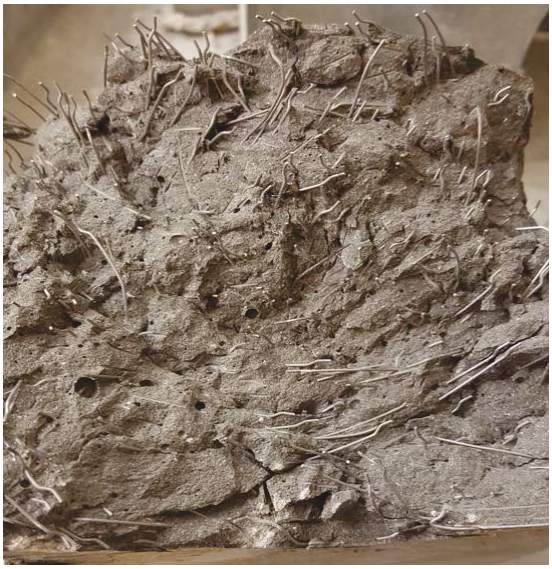

By taking advantage of novel deformation mechanisms, UHPC ductility could be increased beyond traditional void nucleation, growth, and a coalescence of failure modes. Current steel fiber reinforcement does not use all of the energy dissipation mechanisms available for improving UHPC performance. Some of these dissipation mechanisms such as size, shape, and single-fiber pullout have been well-researched. Other

mechanisms such as multi-fiber pullout, bonding mechanisms, plastic deformation, and strain hardening via phase transformation and stress-activated plasticity have been widely left out of the conversation. New energy dissipation mechanisms could be introduced by lowering the yield stress for fibers so that they will undergo plastic deformation and stain harden until they exceed the pullout strength, and then dissipate additional energy via pullout. The tailoring of the fiber strength and mechanical bond to the matrix strength is needed for optimal pullout behavior (Wille and Naaman 2012). Plastic deformation and phase transformation mechanisms have not been investigated for fiber reinforcement in cementitious composites to dissipate energy. Our contribution is the examination of different ductile mechanisms that are possible to increase the fracture toughness of cementitious materials.

1.1.1 Energy dissipation mechanisms of steel fibers

The following subsections will examine the current and potential energy dissipation mechanisms that could be utilized in steel fiber reinforcement.

1.1.1.1 Size and aspect ratio

The physical properties of different types of steel fibers have significant influences on the mechanical properties of UHPC. Scott et al. (2015) looked at four different fiber types within the Cor-Tuf baseline ranging from small rectilinear brass coated (OL) steel fibers to larger hooked-end (3D 55/30 BG) and undulated fibers (Nycon Type V). The purpose of this study was to determine how the change in fibers affected basic quasi-static and impact mechanical properties of UHPC. This study determined that, under flexural and direct tensile conditions, smaller fibers provide significant increase in tensile strength, stress versus strain linearity, and toughness. Larger fibers produced better post-yield load-carrying capacity. This is illustrated in the flexural response plot taken from Scott et al. (2015) in Figure 2. The longer hooked-end and undulated fiber had a more flattened peak at their ultimate load, while the short straight brass-coated fibers produced a sharper more “brittle” peak. Dynamic impact conditions with a “0.50-cal fragment-simulating projectile” produced similar relationships between fiber size and response. Smaller fibers were more effective in reducing residual velocities of projectiles and minimizing mass loss due to cratering and/or spallation than larger fibers. Fiber size did not have a significant impact on perforation or spallation.

Figure 2. ASTM 1609 flexural response from Scott et al. (2015).

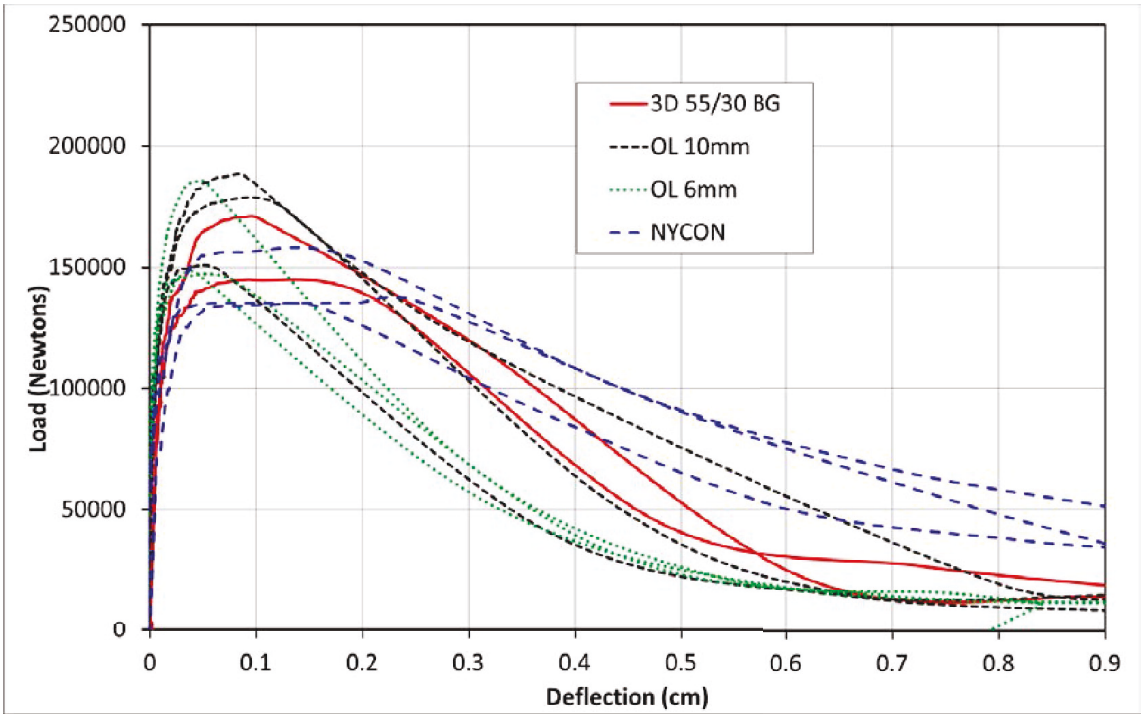

Ryu et al. (2011) conducted a similar study looking at straight and undulated steel fibers with varying lengths while holding diameter at a constant, and thus increasing aspect ratio (fiber length/diameter). They found that increasing aspect ratio by increasing length had little effect on workability and compressive behavior, but improved flexural toughness of UHPC by 30 percent. This would be due to an increase in post-yield load-carrying capacity due to longer fiber lengths being able to hold cracks together for a longer period of time under loading. However, this does not provide a direct correlation between aspect ratio and flexural/tensile performance. If the aspect ratio was to be increased by reducing the fiber diameter, it would provide a higher number density of fibers in a given volume. This could potentially increase flexural/tensile strength without improving toughness similar to the smaller fibers in Scott et al. (2015). Therefore, the aspect ratio alone is not a good indicator of differences in fiber performance. The actual length and diameter must be considered.

1.1.1.2 Fiber deformation mechanisms and pullout

There are several steel fiber designs that are focused on improving the mechanical bond between steel fibers and a UHPC matrix. These designs include hooked-ends, kinks, undulations, twists, etc. All of these designs are meant to provide superior performance versus a rectilinear fiber by

improving mechanical bond strengths and pullout strengths through geometric deformations that provide interlock with the concrete matrix. There are numerous studies on which shapes provide the best fiber performance with no universally accepted optimal deformation mechanism.

A traditional approach for investigating fiber performance within UHPC is through a single-fiber pullout test. This experiment is characterized by partially embedding a fiber within a matrix material, and then pulling the fiber from the matrix while capturing load and displacement. This load-displacement curve can also be considered as a bond versus slip curve when accounting for the embedded surface area (Burchfield 2017).

For straight fibers, the primary failure mechanism is seen in the chemical bond between the fiber and the matrix. For deformed fibers, the mechanical bond adds increased resistance by inducing pressure on the matrix causing increased friction and larger pullout resistance (Wille and Naaman 2012). A typical fiber pullout curve for a straight fiber and a deformed fiber is seen in Figure 3, which demonstrates that a fiber's energy absorption capability is very dependent on the mechanical bond (Naaman and Najm 1991, Burchfield 2017). These tests are well-suited for investigating fiber performance but more specifically the fiber-matrix interfacial bond (Wille and Naaman 2013; Lin et al. 1999; Gray and Johnston 1984; Astarluiglu et al. 2013).

Considerable efforts have been taken to characterize single-fiber pullout mechanisms, but there have been limited investigations into interaction between multiple fibers in a UHPC matrix (Burchfield 2017). Feng et al. (2014) gives an assumption that the cementitious matrix is not significantly affected by fiber pullout due to the fiber creating a tunnel upon pullout with very little matrix damage. Banthia and Trottier (1994) showed evidence that, with higher-strength materials, premature failures occur during pullout due to brittle matrix splitting. This is supported by observations made in Scott et al. (2015) for posttest flexural beams that still had a vast majority of fibers with intact mechanical deformation mechanisms due to brittle matrix splitting. A better understanding of multiple fiber-to-fiber interactions across voids and within UHPC matrices is necessary to fully understand the enhancements provided by fiber reinforcement.

Figure 3. Typical fiber pullout behavior for smooth and deformed fibers (Naaman and Najm 1991).

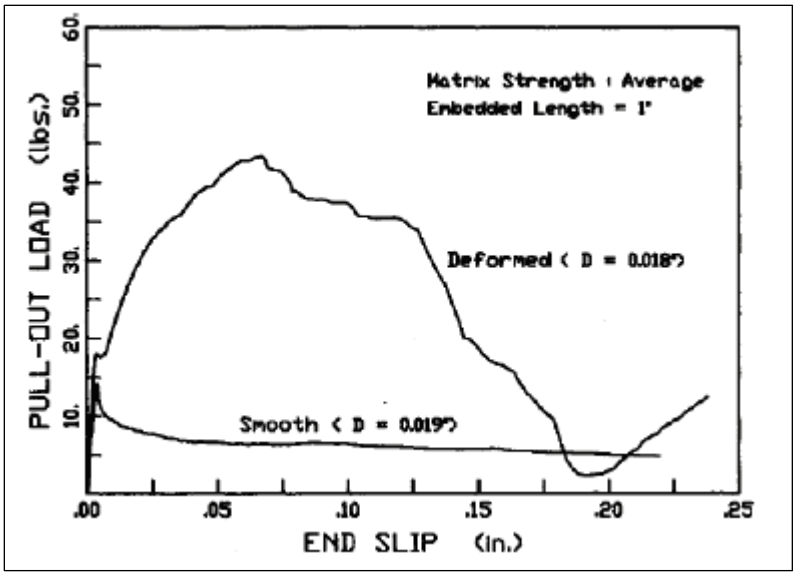

1.1.1.3 Bonding mechanisms

Another potential way to improve toughness in UHPC is to increase the bond strength between the steel fiber reinforcement and the cementitious matrix and, thus, improve the pullout strength. Interfacial transition zones (ITZs) between a steel fiber and the cementitious matrix or a fiber and a nearby aggregate can be a "weak link" in normal concrete. Numerous researchers have shown that lower water-to-cement ratios and high inclusions of silica fume improve ITZ hardness and bonding due to improved particle packing, chemical hydration, and reduced porosity (Wu et al. 2016, Chan and Chu 2004, and Wang et al. 2009).

By nature, UHPCs tend to have high hardness in the ITZs, meaning that the in-situ ITZs around the fibers tend to show brittle behavior similar to that seen in unreinforced UHPCs. This is one explanation for the still-intact fibers seen in Figure 1. Possible ways to improve the bond and counteract the in-situ brittleness would be to coat the fibers with an enamel coating or chemically etch the fibers. Chemical etching is a way to increase friction between fiber and cementitious matrix by creating 'pits' that the concrete can ingress and latch onto at the microscopic level (Naaman 2003). This bonding mechanism could also be considered a deformation mechanism.

Enamel coatings have been studied for use with traditional steel rebar reinforcement and have shown more effective stress transfers from

concrete to steel rebar due to more gradual transitions in microstructure and improved corrosion resistance (Yan et al. 2016, Tang et al. 2012, Yan et al. 2012, and Allison et al. 2012). Enamel coatings have largely gone unstudied in steel fiber reinforcement due to difficulty in getting a consistent even coating on the fibers during the manufacturing process. Although there is a potential for further research and improvement in bonding mechanisms for UHPC, that will not be the focus of this research.

1.1.1.4 Plastic deformation

A plastic or permanent deformation of a steel fiber in UHPC begins after the matrix reaches its yield strength and begins to fracture, typically in tension. Upon fracturing of the matrix, the fibers are then responsible for carrying the load between the two sides of a void. The mechanical properties of the fibers are then directly responsible in determining the toughness of UHPC. However, there have been no studies into how a differing strength and ductility of a fiber can influence the overall performance of the matrix. Current research shows only that the inclusion of fibers improves toughness when compared to UHPCs without steel fiber reinforcement, or between different sizes and shapes of fibers.

A fiber that is too weak would likely undergo plastic deformation without adding toughness to its parent matrix. Standard commercially available alloys often improve UHPC toughness but do not undergo plastic deformation or pullout due to brittle matrix splitting. If the fibers are too strong and do not undergo plastic deformation, there is a reduction in added displacement due to the lack of elongation in the fibers, and the matrix will fracture instead of undergoing fiber pullout further reducing displacement. Fiber alloys that have a strain-hardening capability could allow for the additional displacement by undergoing plastic deformation and then strengthening until reaching the pullout strength and continuing energy dissipation via pullout. More research is needed to determine optimal alloy strengths and if added displacement due to plastic deformation of the fibers does indeed improve UHPC toughness.

1.1.2 Phase transformation and stress activated plasticity

Novel alloys can exhibit stress-activated plasticity mechanisms that increase strength and toughness during plastic deformation. These deformation mechanisms could be utilized to improve the performance of composite materials and increase energy dissipation. By controlling the

chemical compositions of the steel materials that are to be used as steel fiber reinforcement so that it is "metastable" means that, at room temperature, it can easily undergo phase transformations initiated by external loads. This report looks at a stainless steel fiber and an annealed carbon steel fiber in an attempt to improve upon the deformation and energy dissipation mechanisms within UHPC.

Figure 4 shows a theoretical fiber tensile property compared to some carbon steel fibers tested by Rivera-Soto et al. (2016). This fiber yields and then begins to strain-harden via transformation during plastic deformation. Upon yielding and crack formation of the UHPC matrix, the fibers would plastically deform enacting a phase transformation that would strain-harden the fiber until it exceeded the pullout strength and then continues to dissipate additional energy via pullout.

Figure 4. Theoretical optimal fiber tensile strength plot.

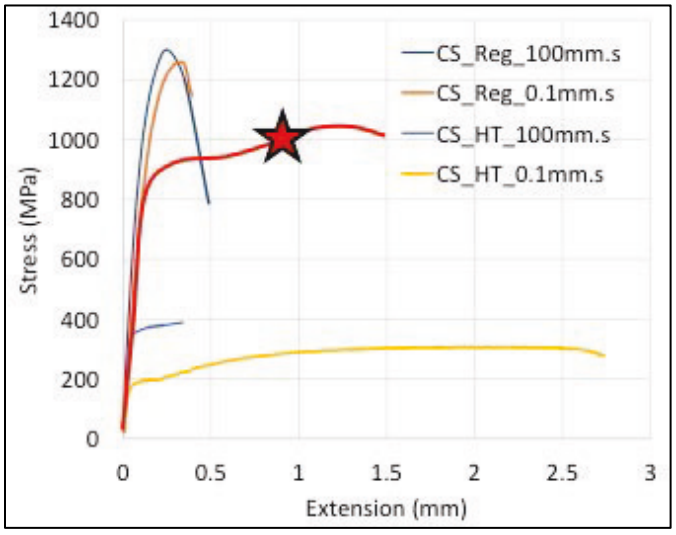

1.2 Research scope

In order to address the privation of information related to alloy selection and heat treatment effects on steel fiber reinforcement in UHPC, this study investigated two common steel fibers of varying alloys along with heat-treated counterparts for each in a consistent matrix. The two fiber types included one carbon steel fiber and a stainless steel fiber of similar size and shape. The testing also included a heat-treated version of the carbon steel fiber and a heat-treated version of the stainless steel fiber. The experimental program included the quasi-static properties of UCS and flexural response. Dynamic testing included penetration testing using

fragment-simulating projectiles. The overall goal of this project was to identify the energy dissipation capabilities of varying alloys and discuss how this type of research could improve the performance of UHPC in different expected loading conditions.

2 UHPC Materials and Thermal Processing

Ultra-High Performance Concrete (UHPC) is a class of concrete that exceeds 140 MPa with high durability due to negligible interconnected porosity. In order to obtain these properties UHPCs are made with specific high-quality materials including but not limited to: oil-well or low-heat portland cement, i.e., with large mean particle size, high C2S content, and low C3A content, siliceous or aluminous fine aggregates, crushed quartz or some other micrometer-sized powder, silica fume, water, high-range water reducing admixtures to control rheology, and other components that vary by manufacturer. Concrete tends to exhibit more brittle-like behavior with higher compressive strengths. This 'brittleness' is offset by the inclusion of steel fibers that aid in delocalizing micro and macro cracking leading to improvements in tensile strength.

2.1 UHPC materials

The UHPC materials used in this study were held consistent except for the steel fiber reinforcement. Overall, four fiber conditions were studied: Carbon Steel (CS), Stainless Steel (SS), Annealed Carbon Steel (AC), and Annealed Stainless Steel (AS). All mixtures were batched in a high-shear rotating pan mixer in 2.5 cubic ft quantities.

2.1.1 Cor-Tuf baseline UHPC

Cor-Tuf Baseline (CTB) is one formulation of UHPC developed by the U.S. Army Engineer and Research Development Center (ERDC) under the name Cor-Tuf. This family of UHPCs is a result of more than three decades of work and investigation into the use of UHPCs and the creation of subsequent adaptations to better suit the material for a variety of applications for both military and civil infrastructures (Scott et al. 2015).

CTB typically has an unconfined compressive strength (UCS) between 28 and 32 ksi (193 to 220 MPa) and a density of approximately 160 lb/ft3 (2563 kg/m3). With this high strength, CTB (as well as most other UHPCs) has a high brittleness that can be counteracted by the inclusion of randomly distributed steel fibers. A detailed history of the development of Cor-Tuf can be found in Green et al. (2014).

Part of the CTB production included a consistent curing regime and testing age of each of the test matrices. The curing regime consisted of seven days of 72°F curing inside a fog room with 100 percent humidity followed by seven days of steam curing at a temperature of 190°F (90°C). The concrete temperature should have negligible effects on fiber alloy conditions. The testing age of each CTB matrix was 28 days.

2.1.2 Steel fiber types

Two hooked-end fiber types were chosen for this study. The 3D 55/30 BG carbon steel fiber and 3D 80/30SL stainless steel from Bekaert fiber types were chosen for their ease of availability and their generic alloy composition. Applied Technical Services performed an analysis according to ASTM E1479 (ASTM 2016b) and ASTM E1019 (ASTM 2011), and results can be seen in Table 1 along with the results for the stainless steel fibers.

Table 1. ASTM E1479-16 analysis of steel fiber reinforcement.

ASTM E1479-16 Analysis of CS Fibers									
Identification	C	Mn	P	S	Si	Cr	Ni	Mo	Cu
1006 Carbon Steel Req.	0.06 Max	0.35 Max	0.040 Max	0.050 Max	n/a	n/a	n/a	n/a	n/a
CS-Fiber	0.06	0.28	0.011	0.002	0.09	0.04	0.03	0.01	0.04
ASTM E1479-16 Analysis of SS Fibers									
Identification	C	Mn	P	S	Si	Cr	Ni	Mo	Cu
304 Stainless Req.	0.08 Max	2.00 Max	0.045 Max	0.03 Max	1.00 Max	18.0 - 20.0	8.0 - 10.5	n/a	n/a
SS-Fiber	0.08	1.06	0.035	0.003	0.4	18.1	8.3	0.02	0.13

The 3D 55/30 BG fibers seen in Figure 5 meet the chemical requirements for 1006 carbon steel. The 3D is an acronym used by the company to illustrate a single hook on the ends of the fiber. The 55 denotes a rounded-up aspect ratio. The fibers are 0.55 mm in diameter and 30 mm long. BG stands for Bright Glued. These fibers come glued together with water-soluble glue that is broken down during mixing. The given tensile strength is 1,345 MPa. The Young's modulus is 200,000 MPa. These fibers had to be washed and dried to remove the glue prior to thermal processing. These fibers will be referred to as CS (carbon steel) throughout the remainder of this study.

Figure 5. Bekaert Dramix 3D 55/30 BG fibers (Williams et al. 2009, Roth et al. 2010).

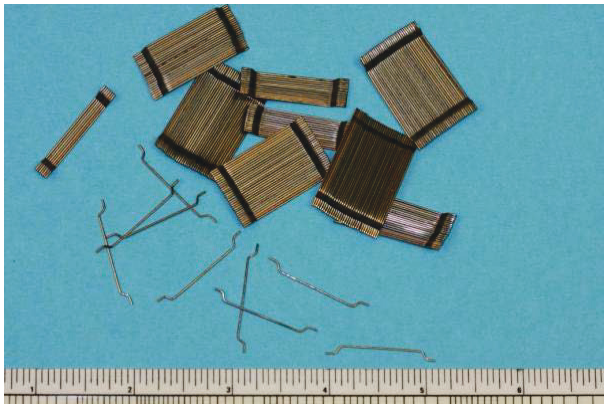

The other fiber type is called 3D 80/30 SL (formerly known as RL- 80/30 SN). Chemical analysis of this fiber shows that it meets the definition of a 304 stainless steel. This stainless steel fiber has a single hook on each end. The 80 represents a rounded-up aspect ratio. The fibers are 30 mm long and 0.38 mm in diameter. The S stands for stainless steel and the L stands for loose, meaning not glued together. The given tensile strength is 2,000 MPa. The Young's Modulus is 200,000 MPa. This stainless steel fiber was the most similar in size to the carbon steel fiber that could be reasonably obtained for this study. These fibers will be referred to as SS (stainless steel) fibers throughout the remainder of this study.

2.2 Thermal processing

In order to modify stress strain behavior of the steel fibers, many thermal processing parameters and their influence on mechanical behavior and fracture mechanisms were studied by Rivera-Soto et al. (2016).

Thermal processing efforts were limited to a Carbolite Elf 11/23 Benchtop Lab Furnace with an 1100°C maximum temperature. The internal furnace dimensions measured 235 x 235 x 400 mm. The relatively small furnace space limited fiber heat treatment production to a rate of 1 lb per batch. Two pans were used with approximately a half-pound of fibers in each pan as seen in Figure 6. A total of 60 batches were needed for the concrete mixture proportions and fiber characterization testing. Despite best efforts, this small batch-by-batch effort produced a relatively high variability between the tensile properties of the heat-treated fibers versus the fibers tested as manufactured. The process could be improved upon with a larger furnace capacity with the capability of heating all fibers in a continuous and even fashion. Fibers from every fifth batch were used for fiber tensile testing.

Figure 6. Thermal processing of CS fibers.

2.3 Thermally processed materials

Two heat treatments were identified, one CS and one SS, during the work by Rivera-Soto et al. (2016) as providing drastically increased ductility of the fibers. The CS heat treatment consisted of annealing the 3D 55/30 BG fibers for 6 min at a temperature of 800°C. The annotation AC (annealed carbon) refers to these fibers. The stainless steel heat treatment was conducted on the 3D 80/30 SL fibers at 1,000°C for 6 min, and will be referred to as (annealed stainless).

The reduced strength of the AS fibers paired with the small diameter of the fiber caused the AS fibers to bend and deform during the UHPC mixing process. This resulted in the fibers nesting together and forming a large tangled fiber ball. This UHPC mixture had to be thrown out and could not be further evaluated. However, the fiber was still used as a reference for the phase transformation section.

3 Experimental Methods

The mechanical property characterization testing was consistent for all fiber conditions. Testing of specimens was performed at quasi-static and dynamic strain rates using the methods described in the following sections. An additional magnetivity characterization was performed on the SS samples to identify the potential for phase transformation.

3.1 Quasi-static mechanical properties

The quasi-static mechanical properties were determined according to their respective ASTM standards with exception of tensile testing the steel fibers that do not fall under a specified method. The steel fiber tensile test method is described in the following section.

3.1.1 Steel fiber tensile testing

Tensile testing was conducted using an Instron E300 at a quasi-static strain rate of 0.00001 s^{-1} in order to determine the ductility and strength of each fiber type. The samples were tested as received and after heat treatment. Each fiber's hooked-end was aligned with the clamping direction, and small aluminum coupons were used to assist in maintaining a consistent gage length.

3.1.2 Unconfined compressive strength

The unconfined compressive strength (UCS) was determined in accordance with ASTM C39 (ASTM 2017). Fiber content generally has little effect on the pre-cracking UCS (Ryu et al. 2011, Hassan et al. 2012, Scott et al. 2015). These tests allow a comparison between the matrices of each Cor-Tuf batch.

3.1.3 Flexural response

The flexural response testing was performed according to ASTM C1609 (ASTM 2012) and is seen in Figure 7. This test used a beam with four-point loading. The cast beams were 101.6 by 101.6 by 457.2 mm and were cast according to ASTM C192 (ASTM 2016a). They were tested on a 406.4-mm support span. Linear variable differential transformers (LVDTs) were used to measure centerline displacement that was, in turn, paired with the corresponding load data to provide a plot of load versus displacement.

Figure 7. ASTM C 1609 for 101.6- x 101.6- x 457.2-mm flexural response beam.

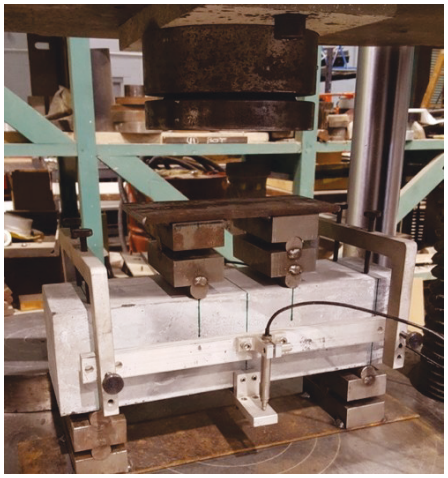

3.2 Dynamic penetration using fragment-simulating projectiles

Direct impact penetration experiments were conducted using a 0.50-caliber fragment-simulating projectile (FSP) to examine the resistance of the UHPC panels to small projectile penetration. A single projectile was fired at each panel with approximately the same impact velocity in each test. Each direct-fire experiment measured impact velocity, the residual velocity of the projectile in the event of perforation, and the final damage state of the target. Multiple posttest photographs of each panel were obtained to record the final damage state. Samples of the UHPC panels were cast to a uniform 30.5-cm by 30.5-cm (12-in. by 12-in.) size with thicknesses of 2.54 cm, 5.08 cm, and 6.35 cm (1.0, 2.0, and 2.5 in.). A set of three panels was generated for each thickness resulting in 12 panels for each fiber type. The desired impact velocity was approximately 1067 m/s (3,500 ft/sec). This combination of panel thicknesses and impact velocity was chosen because it had previously generated damage states and responses that varied from complete perforation of a panel to only cratering of the impact side of the panel (Reinhart and Thornhill 2010). All direct-fire experiments were conducted in ERDC's small-arms ballistic testing facility. This included a cartridge preparation area that contained the proper equipment to hand-load numerous cartridges. The range from muzzle to target in this experimental program was approximately 4.572 m (15 ft). A Physics Applications Inc. small-arms receiver with a sliding return-to-zero base was used to fire the projectiles. The gun included a 1.524 m (5 ft) smooth-bore barrel and was cartridge fired.

Projectile velocity measurements were made using a set of Oehler Research Inc. Model 35P proof chronographs, each connected to two Oehler Model 55 light screens.

The light screens attached to each chronograph were positioned 3 ft apart to capture projectile velocities. Four chronograph screens were positioned between the gun and the target to estimate the impact velocity. The velocity was measured between pairs of the screens, and an estimated impact velocity was generated for each test based on these measurements. A single pair of screens was positioned approximately 4 ft behind the test specimens, as shown in Figure 8, to measure exit (residual) velocities for each experiment. All experiments were conducted with 0-deg obliquity, or perpendicular impact. Samples were mounted in a rigid steel fixture. Panels were held in position by tension in a threaded rod. Rubber padding reduced the contact stresses between the panels and the fixture. The dynamic penetration test set-up can be seen in Figure 8.

Figure 8. Dynamic penetration test set-up (FSP – TL, Full test set-up – TR, Impact velocity chronographs – BL, Concrete panel with witness panel and residual velocity chronographs – BR).

3.3 Vibrating specimen magnetometer

A Versa Lab by Quantum Design Inc. vibrating specimen magnetometer was used to determine whether an SS fiber sample taken from a posttest UHPC specimen had undergone phase transformation and to what extent that transformation had occurred under the dynamic and quasi-static

loading conditions presented earlier in this report. “The magnetic properties of a material are usually characterized by a hysteresis loop, which gives the behavior of a material when excited by an external magnetic field” (Mumtaz et al. 2004). This method is used to analyze the volume fraction of the ferromagnetic phase α’ of a given sample and is calculated by dividing its magnetization saturation in emu/g by the intrinsic magnetization saturation of martensite that ranges from 130 to 160 emu/g (Mongonon and Thomas 1970, Childress et al. 1988).

4 Experimental Results and Discussion

4.1 Steel fiber tensile properties

The average ultimate strengths for the AC fibers were 400 MPa with a standard deviation of 23.73 MPa. The extension to failure for the carbon steel fiber increased from a 0.5-mm average max elongation to an average of 2.3 mm for the AC with a standard deviation of 0.36 mm. The ultimate strength of the CS decreased from approximately 1200 MPa to 400 MPa for the AC.

The average ultimate strength for the AS fibers were 449 MPa with a standard deviation of 6.56 MPa. The stainless steel ultimate strength decreased from approximately 2200 MPa to 450 MPa for the AS. The extension to failure for the stainless averaged 6.10 mm with a standard deviation of 0.50 mm. These results are seen in a load versus elongation plot in Figure 9. The relatively high deviations for the heat-treated fibers are due to the batch-by-batch annealing method.

The low yield strength of the AS fibers caused the fibers to deform during mixing. However, the amount of strain hardening that these fibers underwent relative to the AC fibers illustrates how different alloys could be used to dissipate additional energy. Their ultimate strengths are the same even with the smaller diameter of the AS fibers. A refinement of the heat treatment to increase the yield strength of the AS fibers is needed for further analysis of these fibers.

Figure 9. Load versus elongation to failure for each fiber type. **Note 0.55-mm diameter for CS and AC; 0.38-mm diameter for SS and AS.

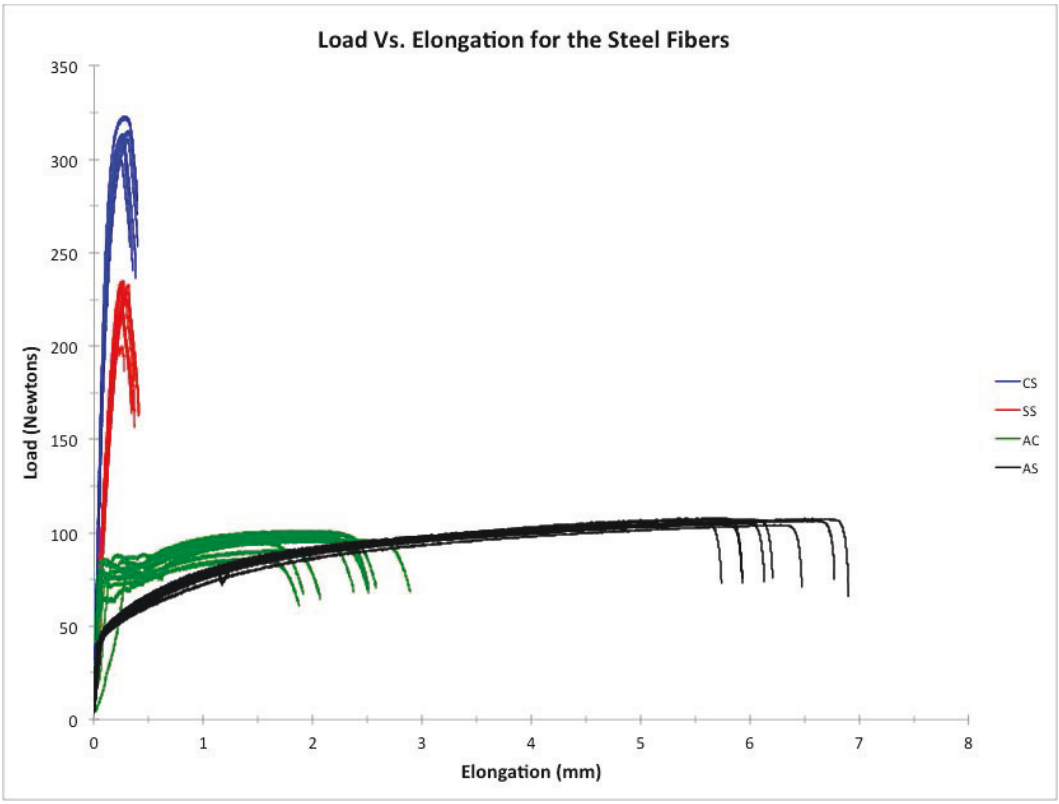

4.2 Quasi-static results

The UCS and Flexural Response results are seen in Table 2. These results are the averages of three tests for each test method with the exception of one of the AC flexural response beam that had a casting defect that led to an uncharacteristically low strength. The SS and AC mixtures had similar compressive strengths of around 225 MPa while the CS mixture had a lower UCS of about 194 MPa. This result is within the typical tolerance historically seen for CTB and is not a result of the CS fibers in that mixture. The ultimate flexural response strength was determined and compared to the UCS. It is shown that higher fiber strengths correlated to higher flexural strengths with the SS having a flexural strength that is 19 percent of the UCS. The CS had a flexural strength that was 16.5 percent of the UCS, and AC having by far the lowest at 8.9 percent.

Table 2. Quasi-static testing results.

Fiber Type	Avg. Unconfined Compressive Strength (MPa)	Standard Deviation of UCS	Max Flexural Strength (MPa)	Standard Deviation of Flexural	Max Flexural Strength of Max Compressive (%)
SS	223.4	5.94	42.5	0.52	19.0
CS	193.7	9.46	32.0	3.75	16.5
AC	225.8	13.69	20.0	0.01	8.9

All three of the fiber treatments showed some comparable yield strengths of the CTB matrix at approximately 70 kN. It is seen in Figure 10 that the fiber's strength and ductility drastically affect the post-yield load-carrying capacity. The AC fibers proved to be too extensible after the annealing process and plastically yielded to failure without any additional ductility or strength being added to the CTB matrix. The AC fibers produced an ultimate strength equal to the yield strength of CTB. A picture of the plastically yielded fibers within the flexural response beam can be seen in Figure 11 along with a picture of post-tested flexural response beams that contain the CS and SS fibers. It is important to notice that the much smoother fracture surface of AC versus the CS and SS. That smooth surface shows that the AC fibers provided little crack propagation resistance. Once a crack nucleated and began propagating through these beams, the crack's interactions with the fiber lead to plastic deformation of the fiber then crack propagation continuation through the plastic deformation of the next fiber until this process led to catastrophic failure of the beam.

Figure 10. Flexural load versus center-line displacement.

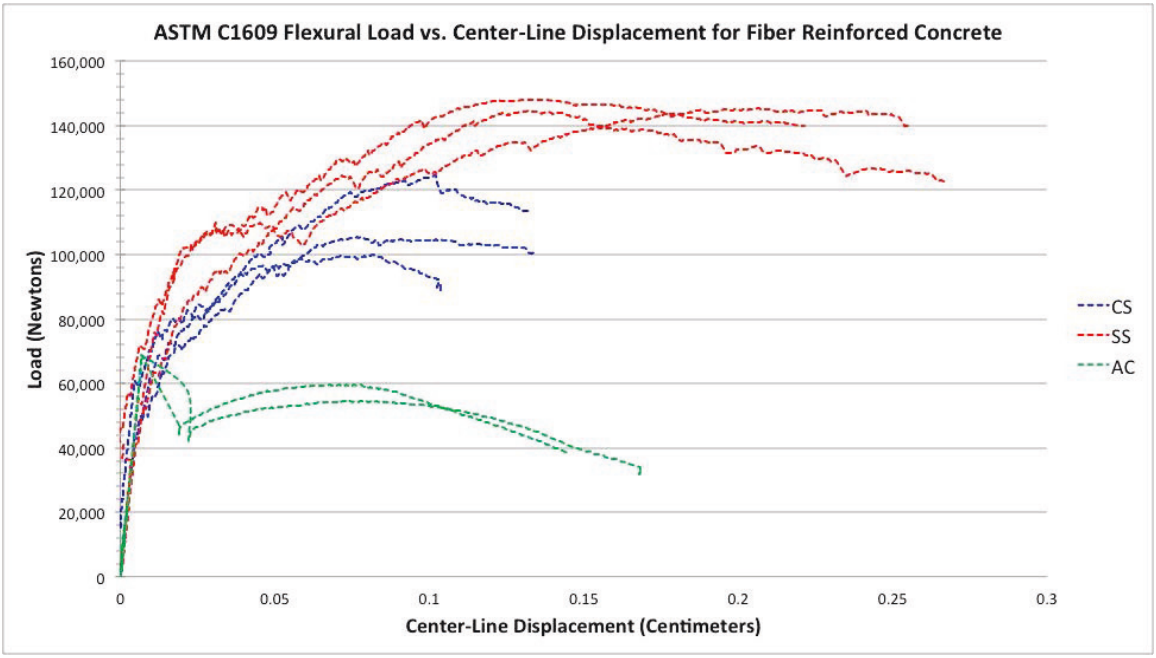

The CS fibers showed improved post-yield load-carrying capacity relative to the AC fibers with an increased displacement to failure as well. These tests were prematurely stopped at a 5 percent drop in load instead of being carried out until overall failure and a load return to zero. Scott et al. (2015) conducted similar tests on these fibers but with a 152.4- x 152.4- x 533.4-mm beam versus the 101.6- by 101.6- by 457.2-mm beams used in this test. Those test loads returned to zero or ultimate displacement at about 0.7 cm of centerline displacement leading the authors to believe that these beams would reach their ultimate displacement at around 0.4 cm. Figure 11 shows a picture of post-test CS flexural response beams with many fibers still intact. This shows that a majority of the fibers do not undergo plastic deformation or pullout, and the crumbling of the CTB matrix around the fiber controls deformation mechanisms. This is similar to the brittle matrix splitting seen in Banthia and Trottier (1994) and Scott et al. (2015). The posttest beam cross section has a very rough surface. The topography of this post-test beam cross section illustrates that during crack propagation, interaction with a fiber would arrest propagation until the crack fractured the matrix enough to essentially bypass or go around the fiber with very few of the fibers deforming or undergoing pullout.

Figure 11. Post-test flexural response beams (101.6 mm x 101.6 mm) (AC - top left, CS - top right, SS - bottom).

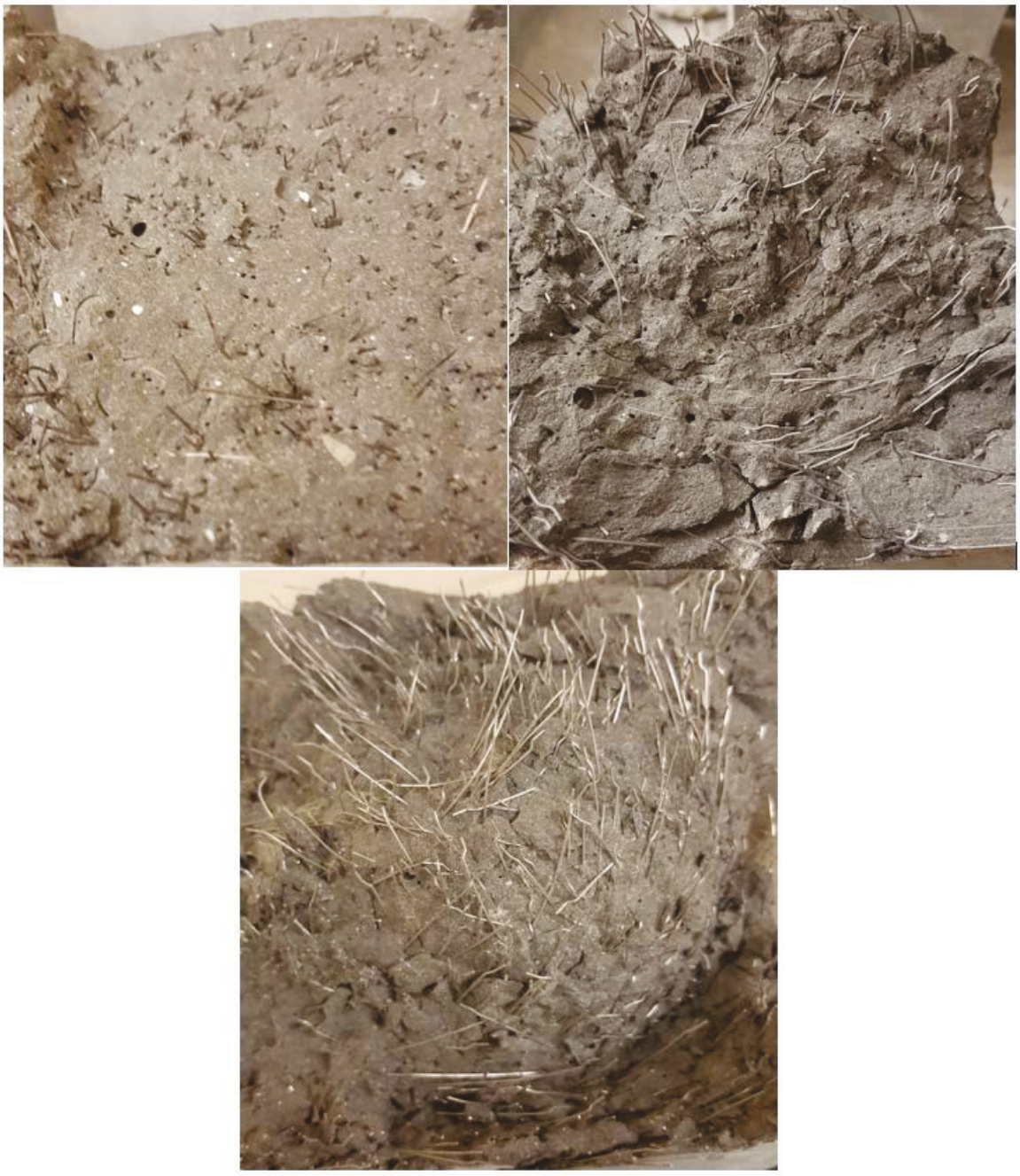

The SS fibers show the best overall strength, energy dissipation, and toughness of these three fiber types. This is partly due to a slight increase in number density, but it is also due to their increased strength and phase transformations that take place during deformation. See Section 4.4 for additional information. These phase transformations occurred during the beam deflection and were confirmed to have happened by using a

Vibrating Specimen Magnetometer (VSM). Transformations occurred during both quasi-static and dynamic testing. Examination of the posttest beam cross section shows a crack propagation pattern similar to the CS beam. The relatively uneven topography of the cross section alludes to a crack propagation that was arrested by the fibers until coalescence around the fiber, causing a matrix fracture that released the fiber from one side of the beam. Very little plastic defamation or pullout of the SS fibers was seen, but the little bit that does occur appears to occur more on the tensile face of the beam.

The large majority of the SS fibers in the fractured area of this beam were in a damaged state similar to the intact fiber meaning the SS fibers in their current state in a quasi-statically loaded UHPC would see an insignificant amount of phase transformation. This is an energy dissipation mechanism that goes largely unused. By harnessing this mechanism using novel alloys in conjunction with other deformation mechanisms such as plastic deformation and fiber pullout along with mechanical deformations like fiber size and shape effects, UHPC strength and toughness could be improved and potentially tailor-fitted to their expected loading conditions.

4.3 Dynamic penetration results

Direct-fire experiments were conducted using a 0.50-caliber fragment-simulating projectile (FSP) to examine the resistance of the UHPC panels to small projectile penetration. Samples of the UHPC panels were cast to a uniform 30.5 cm by 30.5 cm (12 in. by 12 in.) size with thicknesses of 2.54 cm, 5.08 cm, and 6.35 cm (1.0, 2.0, and 2.5 in.). This section will discuss the results of this penetration experiment.

4.3.1 2.54-cm-thick panels

The fiber variance did not prevent perforation for any of these three fiber types.

The CTB panels containing the CS fibers produced the highest residual velocity averaging around 20 m/s higher than the SS or AC fibers. The CS fibers also had a residual velocity approximately 2 percent higher relative to the impact velocity than the SS or AC fibers. A graphical interpretation of the residual velocities for the 2.54-cm- and 5.08-cm-thick panels is shown in Figure 12. It is worth noting that Shot #2 for the CS fiber appears to be an outlier with a higher residual velocity than any other test at this

thickness with every other recorded residual velocity coming between 41 and 42.5 percent. Two of the shots, CS shot #11 and AC shot #10, had chronograph errors during testing and were unable to show residual velocities.

Figure 12. Post-impact projectile for the SS 5.08-cm panel shot #6.

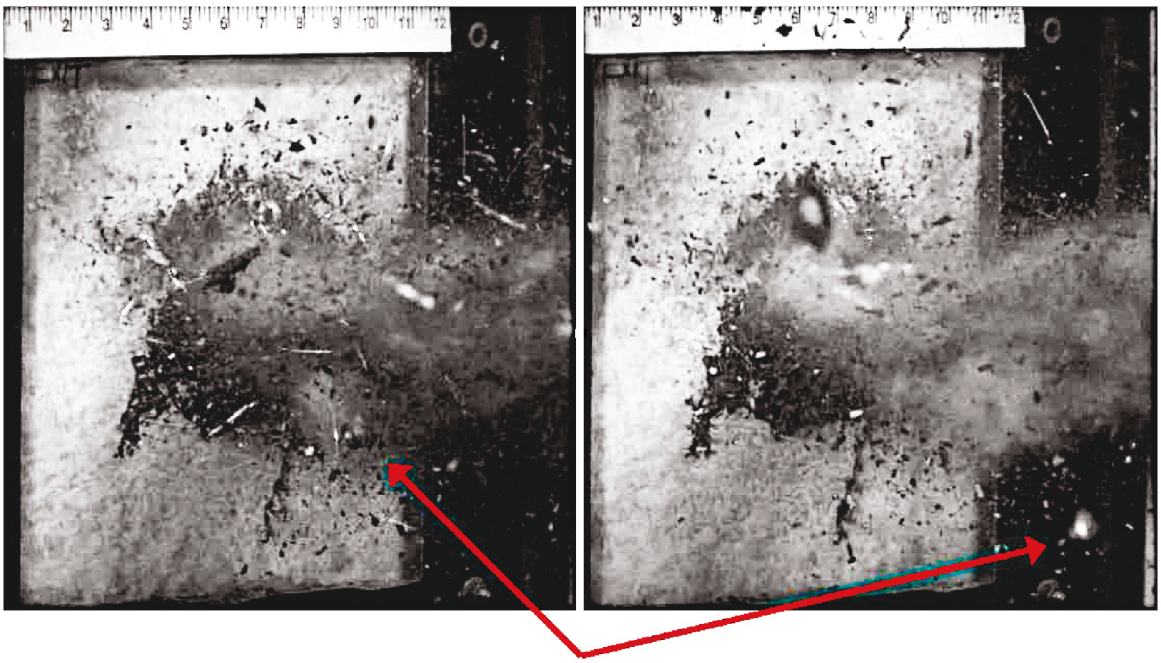

Overall, the difference in fiber strength and ductility showed no difference in failure mechanisms that could prevent or improve perforation or fragmentation of the 2.54-cm panels. High-speed video recordings of each shot were analyzed, and little to no difference in failure mechanics was seen visually for each of the fiber conditions. Every panel was fully perforated and produced a damage zone with a debris field of roughly the same size. Every panel had a mass loss of between 2.34 and 2.85 percent. The CS panels had the lowest average of 2.42 percent, followed by the SS with a 2.58-percent average mass loss, and the AC panels having the highest at 2.68 percent. There appears to be no trends, and this difference could be attributed to noise in the tests. More testing would be needed to identify any trends in perforation, fragmentation, and mass loss for this panel thickness. The testing results for each 2.54-cm panel shot are in Table 3.

Table 3. Dynamic impact results for 2.54-cm-thick panels.

Shot #	Sample Description	Impact Velocity (m/s)	Residual Velocity (m/s) 2.54 cm-thick Panel	% RV Relative to the IV	% Weight Loss	Notes
11	CS	1,071	N/R	N/A	2.340	Chronograph Error - Residual velocity not recorded.
2	CS	1,080	498.72	46.18	2.396	No Witness Panel
20	CS	1,041	427.17	41.03	2.523	Low impact velocity. Witness panel used to minimize spall passing through chronograph screens.
	Average CS/ Std. Dev		462.94 / 50.59	43.61	2.42 / 0.094	
21	SS	1,065	450.80	42.33	2.388	Witness panel used to minimize spall
3	SS	1,074	440.74	41.04	2.847	No Witness Panel
12	SS	1,052	439.43	41.77	2.496	Witness panel used to minimize spall.
	Average SS/ Std. Dev		443.66 / 6.22	41.71	2.58 / 0.24	
19	AC	1,072	440.37	41.08	2.689	Witness panel used to minimize spall
10	AC	1,082	N/R	N/A	2.828	Chronograph Error - Residual velocity not recorded.
1	AC	1,062	446.03	42.00	2.519	No Witness Panel
	Average AC/ Std. Dev		443.20 / 4.00	41.54	2.68 / 0.16	

4.3.2 5.18-cm-thick panels

The 5.08-cm panel thickness resulted in some data seen in Table 4 that, while interesting, does not provide any trend that aligns with the data for the 2.54-cm-thick panels. The most intriguing aspect of these data is a residual velocity of zero for the SS panels, while the CS and AC panels each showed low residual velocities in the 25-70 m/s range. Inspection of the SS panels showed that, in fact, all of the panels were perforated. The projectile for shot #6 can be seen in the high-speed video recording. Screen shots from this video are shown in Figure 12. The projectile comes into view well after the initial spall has left the video frame. The projectile

is on a relatively slow downward path. It is 'mushroomed' from the impact and rotating axially as a rifled projectile typically does, but on a wobbled spiral as it exits the bottom right side of the frame. The projectile could also be seen in shot #24, but direction could not be quantified due to the debris field. It was concluded that, upon impact, the SS panels caused the projectile to deter from its path far enough to cause the projectile to impact the witness panel prior to reaching the chronograph for a residual velocity measurement. This was corroborated by the presence of relatively large elongated punctures on the witness panels. Post-impact projectiles could be seen in high-speed video recordings for AC shots #13 and #4. They maintained their original trajectory. No post-impact projectiles could be seen for CS panels. The sizes of the debris fields appear to be related to the mass loss for each individual panel and not the fiber type.

Table 4. Dynamic impact results for 5.08-cm-thick panels.

Shot #	Sample Description	Impact Velocity (m/s)	Residual Velocity (m/s) 5.08 cm-thick Panel	% RV Relative to the IV	% Weight Loss	Notes
14	CS	1,065	59.78	5.61	4.05	Witness panel used to minimize spall passing through chronograph screens.
5	CS	1,067	Spall (341.83)		4.72	No Witness Panel
23	CS	1,052	27.69	2.63	3.61	Witness panel used to minimize pall
	Average CS/Std. Dev		43.73 / 22.69	4.12	4.12/0.56	
24	SS	1,034	0.00	0	5.30	Low impact velocity.
6	SS	1,076	Spall (347)		3.96	No Witness Panel
15	SS	1,061	0.00	0	3.56	Witness panel used to minimize spall
	Average SS/Std. Dev		0.00 / 0.00	0	4.27/0.91	
22	AC	1,067	68.88	6.46	3.00	Witness panel used to minimize spall
13	AC	1,053	49.38	4.69	3.86	Witness panel used to minimize spall
4	AC	1,078	Spall (341.83)		3.35	No Witness Panel
	Average AC/Std. Dev		59.13 / 13.78	5.575	3.40 / 0.43	

At this panel thickness, the AC panels had the lowest mass loss of 3.4 percent. This was about three-quarters of a percent less than the CS and SS panels that had roughly the same mass loss at around 4.2 percent with the SS panels having one potential outlier that skewed its average higher. Removing that data point gives an average residual velocity of 3.76 percent for the SS fibers. At this point, residual velocity and mass loss appear to have an inverse relationship for both the 2.54-cm and 5.08-cm thicknesses. The AC panels had the highest residual velocities around 60 m/s, and the CS panels averaged around 43 m/s with a much higher variance between the reported values. While the residual velocities were not identified for the SS panels due to their deterred flight path, it is expected that these velocities would have been the lowest of each panel type. A graphical representation of residual velocities for 2.54-cm and 5.08-cm thicknesses is shown in Figure 13.

Figure 13. Graphical representation of average residual velocities (m/s) for 2.54-cm and 5.08-cm-thick panels.

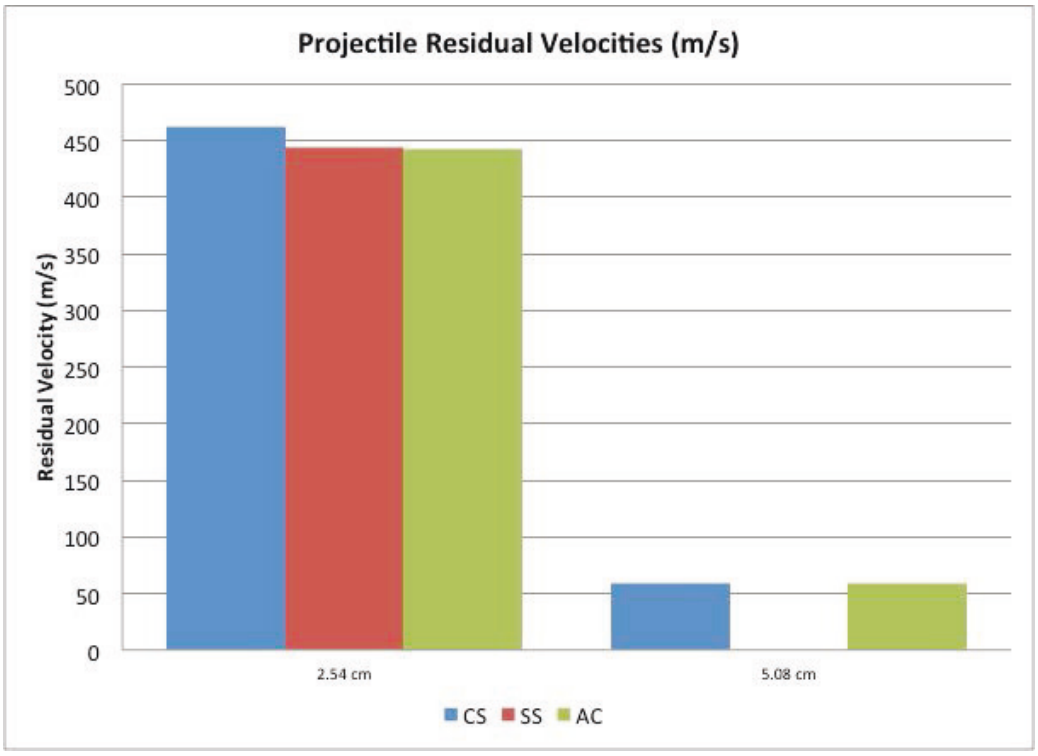

4.3.3 6.35-cm-thick panels

None of the 6.35-cm-thick panels were perforated regardless of the fiber strength or ductility. High-speed video recordings were taken for each of the 6.35-cm panels, and video analysis for this panel thickness showed some differences in the fracture mechanisms for each of the fiber types. An impact crater and exit-face spall craters were present for every panel except two of the SS panels. These two panels showed backside damage and cracking that produced 2-3 damage sections, but with no large spallation and the lowest mass loss for any panel. This can be seen in Figure 14 for shot #18. Shot #9 that produced backside spall for the SS panel reluctantly pulled away from the panel in two large sections. Scott et al. (2015) concluded in a similar test set-up that smaller fibers with higher densities' values were more effective in minimizing mass loss due to cratering and/or spallation. However, the mass loss difference between the 3D 55/30 BG and the small brass coated OL 0.6-mm diameter and 10-mm in length fibers was very minimal. Their conclusion was based mostly between the OL brass coated fibers and the Nycon Type V fiber that is much larger than the 3D 55/30 BG. The 3D 55/30 BG fibers and the 3D 80/30 SL fibers are even more similar in size. Therefore, these data coupled with the residual velocity measurements for the 5.08-cm panels suggests that the SS fiber strength and phase transformation reduced spallation and residual velocities (when applicable) under dynamic impacting conditions.

The AC panels had a relatively large variance in mass loss as seen in Table 5, but each AC panel outperformed the CS panels in the mass loss metric. The added fiber ductility assisted in holding onto some of the larger spalls whereas the CS panels did little to prevent spall. The AC panels appeared to have more of a peeling motion from the impact zone instead of the straight detachment and spallation that projected from the impact zone that the CS panels underwent. The added ductility and reduced strength allowed the AC fibers to plastically deform during this dynamic penetration event rather than the fiber staying rigid and fracturing the CTB matrix, and then debonding from it.

Figure 14. Exit face spall for 6.35-cm panels (CS Shot #08 -TL, SS Shot #18 -TR, AC Shot #26 -B).

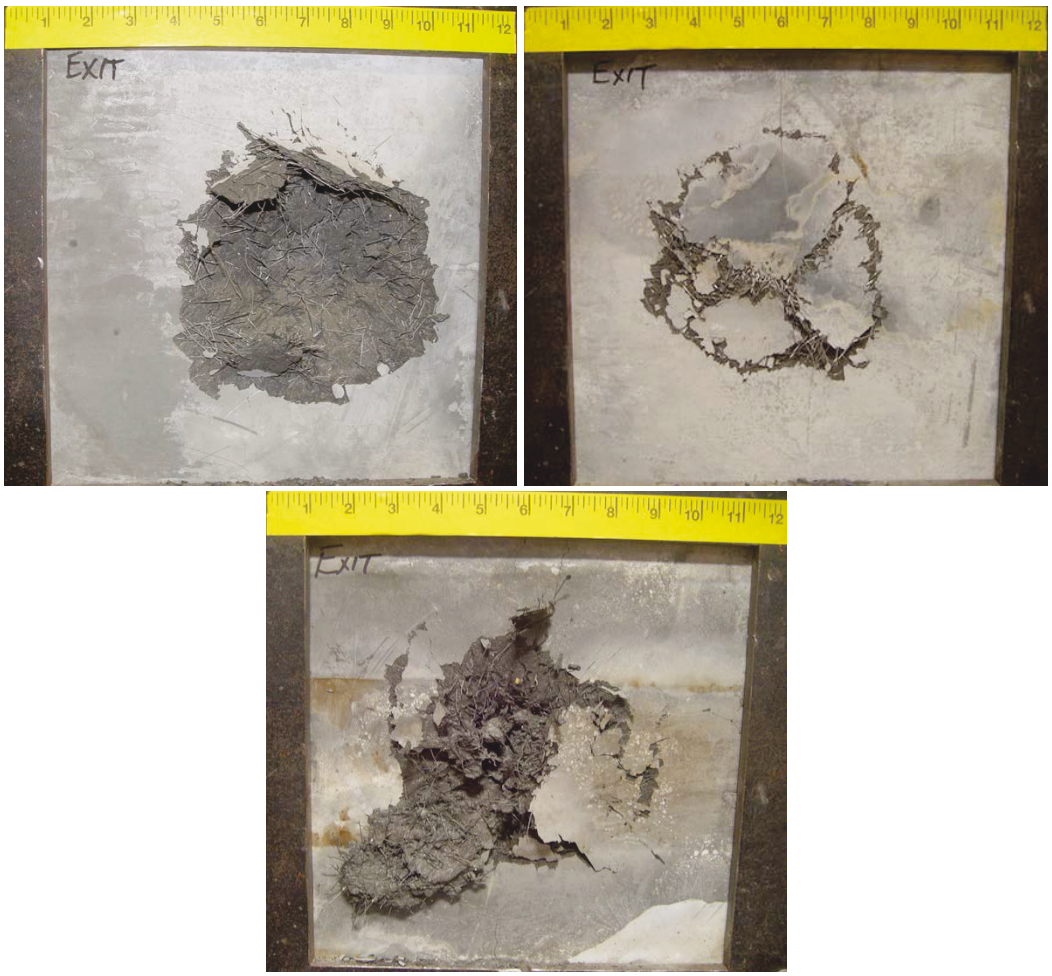

Table 5. Dynamic impact results for 6.35-cm-thick panels.

Shot #	Sample Description	Impact Velocity (m/s)	% Weight Loss	Notes
17	CS	1,041	3.58	Low impact velocity. Witness panel used.
8	CS	1,065	4.15	Witness panel used to minimize spall passing through chronograph screens.
26	CS	1,077	3.28	Witness panel used to minimize spall
	Average CS/ Std. Dev		3.67 / 0.44	
27	SS	1,048	1.24	Low impact velocity. Witness panel used.
9	SS	1,071	4.29	Witness panel used to minimize spall
18	SS	1,045	1.49	Low impact velocity. Witness panel used.

Shot #	Sample Description	Impact Velocity (m/s)	% Weight Loss	Notes
	Average SS/ Std. Dev		2.34 / 1.70	
25	AC	1,068	1.71	Witness panel used to minimize spall
16	AC	1,071	2.44	Witness panel used to minimize spall
7	AC	1,061	3.20	Witness panel used to minimize spall
	Average AC/ Std. Dev		2.45 / 0.74	

4.4 Phase transformation verification

The SS fibers were determined to be an AISI 304 stainless steel, which is a common low-grade stainless that can undergo transformation-induced plasticity (TRIP) mechanisms. It is an austenitic or gamma phase stainless steel that is susceptible to a face-centered cubic (fcc) phase transformation into epsilon and alpha prime phases, which are body-centered cubic (bcc) phases of martensite in steels. The gamma to alpha prime transformation in stainless steels can be induced by plastic deformation at room temperature (Hecker et al. 1982). The plastic deformation results in the transformation of parent austenite (γ) to martensite of hexagonal close-packed and/or body-centered cubic (α´) crystal structures. Such a transformation to martensite during plastic deformation is advantageous as it imparts a good combination of strength and toughness to austenitic stainless steels (De et al. 2004, Mangonon and Thomas 1970). This transformation process has been well-documented to occur in 304 stainless during deformation at different strain rates and temperatures (Hecker et al. 1982, Murr et al. 1982, De et al. 2004, Das et al. 2008), but it has not been documented to occur while being used as reinforcement within a composite or concrete.

Figure 15 shows the hysteresis loop for several samples of the SS fibers. A single control sample was tested along with many samples that were taken from the posttest fractured areas of the SS CTB samples. A sample of the AS fiber was tested to show the magnetization or lack thereof of the fully annealed fibers. One sample each was taken from the perforated areas of 2.54-cm and 5.08-cm panels, and another sample was taken from the impact zone of a 6.35-cm panel. Two more samples were taken from a posttest flexural beam with one of the fibers being visually deformed while the other fiber was visually intact. Each sample was cut into a 3-mm test specimen, weighed, and then mounted into the VSM for testing. The 3-mm

sample was taken from the middle span of the fiber and not from the hooked-end due to a potential for localized transformation at that bend point. The control had a magnetization saturation of 75 emu/g that corresponds to about 52 percent α' marten site assuming an intrinsic value of 145 emu/g. This value may sound high being that 304 stainless steel is considered "austenitic" steel, but makes sense when considering how these fibers are manufactured through a drawing process that reduces the diameter of a stainless steel bar until it reaches the diameter for this fiber of 0.38 mm. The 6-min heat treatment at 1,000°C reduced the amount of α' phase martensite to 7 percent in the AS fiber.

Figure 15. Magnetization saturation for posttest SS fiber samples.

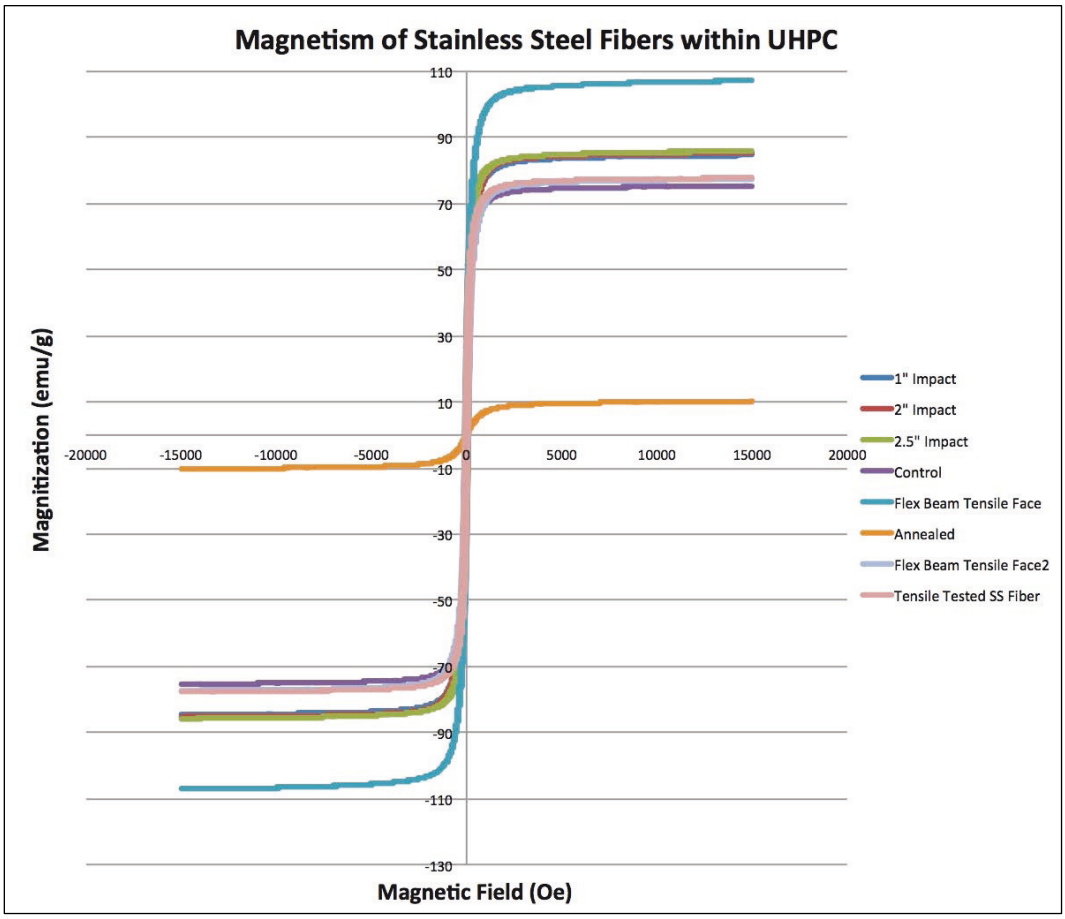

The phase transformations that took place in the posttest CTB specimens shed light onto how fiber reinforcement could be tailor-made for the design function of a UHPC composite and improve the performance of that UHPC member for its specific purpose. The dynamic impact specimens, no matter the panel thickness, all increased in magnetivity by the same amount. The SS fibers sampled from these panels all reached a

magnetization saturation level of around 85 emu/g or 59 percent α' phase martensite. This means that the force imparted on the material by the projectile controls the amount of fiber deformation and phase transformation in the impact area, and it is not influenced by the perforation or lack thereof of the panel. Two fibers were tested from the tensile face of a posttest flexural beam. Each sample yielded a drastically different result. The sample that was taken from a fiber that was visually intact saw a very small amount of martensitic transformation. This sample yielded a saturation value of 77 emu/g and translates to 53 percent of α' martensite composition, which is only a 1-percent increase. The other sample was taken from an obviously deformed fiber in the same tensile face of the same beam. It had a magnetization saturation of 107 emu/g or an almost 74 percent α' martensite composition. It is hypothesized that the dynamic impact tests had a higher strain rate that suppressed the α' martensite transformation due to adiabatic heating in a process similar to what was seen in Talonen et al. (2005), Hecker et al. (1982), and Stout and Follansbee (1986) when compared to the visually deformed quasi-static fiber. However, the lack of plastic deformation in the majority of the SS fibers mitigates the potential for a higher amount of work hardening within the UHPC during quasi-static loading conditions.

5 Future Work

In general, 304 stainless steel is about 4 times the cost of plain carbon steel, while high-strength low-alloy (HSLA) is 1.3 times, Advanced High Strength Steel (AHSS) is 1.55 times, and TRIP is 1.75 times the cost of regular carbon steel. This general estimate does not include the costs of manufacturing these materials into fibers for use in concrete reinforcement. In short, there are other metals that could be looked at as fiber reinforcement that could provide additional energy deformation via the same mechanisms in this report or twinning induced plasticity (TWIP) at much less of a cost than stainless and only slightly higher than carbon steel.

5.1 Meta-stable steels: TRIP and TWIP

It was proven in this report that the SS fibers underwent a phase transformation and transformation induced plasticity (TRIP) during deformation of the CTB matrix at both quasi-static and dynamic load rates. The amount of transformation will vary based on loading conditions and other ambient conditions. TRIP and TWIP have been described as "designations that indicate that a phase transformation within the microstructure has an impact on the mechanical properties of the steel." In stainless steels, these mechanisms are often caused from chromium, nickel, and silicon alloy additions, which are relatively expensive metals that cause the costs of stainless steels to be substantially higher. There are many TRIP and TWIP capable steels that could impart the same mechanisms at a lower cost. The lower cost is largely due to the use of manganese in the steel versions instead of chromium and nickel that is used in stainless steels.

There is a wide availability of TRIP and TWIP steels that can have both high strength and high ductility. These metals are often classified by their dominant deformation mechanism and their ultimate and yield strengths. The fibers in the AC flexural beams failed entirely due to plastic deformation. The fibers in the CS flexural beams, even though they are not TRIP or TWIP capable, failed largely due to the break-up of the fragile matrix around the fiber. This suggests that for CTB, there is a TRIP or TWIP steel that has yield and ultimate strength combination somewhere in between the mechanical properties of those fibers that can enact all the deformation mechanisms of interest.

5.2 Manufacturability

Typical steel fiber reinforcement manufacturing consists of taking an off-the-shelf metal rod and drawing it through a series of dyes until it reaches the diameter specified by the manufacturer. The fibers are then cut to length and crimped or deformed into their desired shape. This is a process that typically does not involve heat treatments and does not quantify the microstructural effect that the drawing process has on fibers. These aspects are not considered largely due to cost and efficiency.

Manufactured phase-transformable steel-fiber reinforcement would likely need to undergo heat treatment either prior to or after the drawing process. This makes alloy selection very important for minimizing this process in order to provide industry with a big enough benefit-to-cost of production ratio to justify use of these materials.

6 Conclusions

The goal of this effort was to prove that a new energy dissipation mechanism could be introduced to UHPC and increase its overall toughness. Current steel fiber reinforcement has limited energy dissipation, and selection of proper heat treatments and alternative alloys can increase the post-yield load-carrying capacity of UHPC for both static and dynamic applications. The testing utilized a laboratory standard UHPC known as Cor-tuf Baseline that was produced using four fiber types. Those fibers included a 3D 55/30 BG carbon steel fiber, a 3D 80/30 SL stainless steel fiber, and two heat-treated versions of those fibers. The heat-treated stainless steel fibers failed during mixing due to a too-drastic reduction in tensile strength, leaving three fiber types to be studied. Based on the results of the experimental investigation, the following conclusions were made.

- Fiber strength and ductility have an important effect on UHPC toughness in both quasi-static and dynamic environments.
- The SS fibers improved flexural strength and displacement to failure due to their increased tensile strength and phase transformation capability. Some of that improvement is also attributed to their slight increase in number density versus the CS fibers. The SS fibers also provided the best dynamic impact resistance.
- The AC fibers were over-annealed. These fibers all plastically deformed in the post-yield flexural beam and reduced the energy dissipation ability of the CTB matrix. However, the increased ductility of these fibers reduced the amount of spall in the CTB panels in the 5.08-cm and 6.35-cm thicknesses. The lower mass loss and video recording of the AC fibers versus the CS fibers evidenced this.
- The VSM verified that phase transformation does occur in phase transformable fibers during post-yield deformation of UHPC. The amount of transformation differs depending on strain rate.

The overall conclusion was that phase-transformable metals could introduce a strain-hardening effect in steel fiber reinforcement that could improve the energy dissipation capability of UHPC. The improved capability would derive from post-yield plastic deformation in the fibers that strain-harden until reaching the pullout strength, and dissipating additional energy via fiber pullout.

References

Allison, P. G., R. D. Moser, C. A. Weiss, P. G. Malone, and S. W. Morefield. 2012. Nanomechanical and chemical characterization of the interface between concrete, glass-ceramic bonding enamel and reinforcing steel. *Construction and Building Materials* 37:638-644.

American Society for Testing and Materials (ASTM). 2011. *Standard test methods for determination of carbon, sulfur, nitrogen, and oxygen in steel, iron, nickel, and cobalt alloys by various combustion and fusion techniques*. Designation: E1019-11. West Conshohocken, PA: ASTM International. https://doi.org/10.1520/E1019-11.

_____. 2012. *Standard test method for flexural performance of fiber-reinforced concrete (using beam with third-point loading)*. Designation: C1609/C1609M-12. West Conshohocken, PA: ASTM International. https://doi.org/10.1520/C1609_C1609M-12.

_____. 2016a. *Standard practice for making and curing concrete test specimens in the laboratory*. Designation: C192/C192M-16a. West Conshohocken, PA: ASTM International. https://doi.org/10.1520/C0192_C0192M-16A.

_____. 2016b. *Standard practice for describing and specifying inductively coupled plasma atomic emission spectrometers*. Designation: E1479-16. West Conshohocken, PA: ASTM International. https://doi.org/10.1520/E1479-16.

_____. 2017. *Standard test method for compressive strength of cylindrical concrete specimens*. Designation: C39/C39M-17b. West Conshohocken, PA: ASTM International. https://doi.org/10.1520/C0039_C0039M-17B.

Astarliouglu, S., T. Krauthammer, and C. Felice. 2013. *State-of-the-art report on fiber-reinforced, ultra-high performance concrete (2nd Edition)*. Center for Infrastructure Protection and Physical Security. Gainesville, FL: University of Florida.

Banthia, N., and J-F. Trottier. 1994. Concrete reinforced with deformed steel fibers, Part I: Bond-slip mechanisms. *Materials Journal* 91(5). doi:10.14359/4059.

Burchfield, C. A. 2017. *Performance assessment of discontinuous fibers in fiber reinforced concrete: Current state-of-the-ar*t. ERDC/GSL TR-17-19. Vicksburg, MS: U.S. Army Engineer Research and Development Center.

Chan, Y-W., and S-H. Chu. 2004. Effect of silica fume on steel fiber bond characteristics in reactive powder concrete. *Cement and Concrete Research* 34:1167-1172.

Childress, J., S. H. Liou, and C. L. Chien. 1988. Magnetic properties of metastable 304 stainless steel with BCC structure. *Journal De Physique* C8-113 – C8-114 (Suppl. 12 T.49). http://dx.doi.org/10.1051/jphyscol:1988843.

Das, A., S. Sivaprasad, M. Ghosh, P. C. Chakraborti, and S. Tarafder. 2008. Morphologies and characteristics of deformation induced martensite during tensile deformation of 304 LN stainless steel. *Materials Science and Engineering: A* 486(1):283-286.

De, A. K., D. C. Murdock, M. C. Mataya, J. G. Speer, and D. K. Matlock. 2004. Quantitative measurement of deformation-induced martensite in 304 stainless steel by X-ray diffraction. *Scripta Materialia* 50(12):1445-49.

Feng, J., W. W. Sun, X. M. Wang, and X .Y. Shi. 2014. Mechanical analyses of hooked fiber pullout performance in ultra-high-performance concrete. *Construction and Building Materials* 69(October):403-10. doi:10.1016/j.conbuildmat.2014.07.049.

Gray, R. J., and C. D. Johnston. 1984. The effect of matrix composition on fibre/matrix interfacial bond shear strength in fibre-reinforced mortar. *Cement and Concrete Research* 14(2):285-96. doi:10.1016/0008-8846(84)90116-9.

Graybeal, B. 2011. *Ultra-high performance concrete*. No. FHWA-HRT-11-038. Washington, DC: Federal Highway Administration.

Graybeal, B. A. 2006. Materi*al property characterization of ultra-high performance concrete*. FHWA-HRT-06-103. Washington, DC: Federal Highway Administration.

Green, B., R. Moser, D. Scott, and W. Long. 2014. *Ultra-high performance concrete history and usage by the United States Army Engineer Research and Development Center*. *ASTM Special Technical Publication 1581*. ASTM C09 Symposium on Ultra-High Performance Concrete. West Conshohocken, PA: ASTM.;

Hassan, A. M. T., S. W. Jones, and G. H. Mahmud. 2012. Experimental test methods to determine the uniaxial tensile and compressive behaviour of Ultra High Performance Fibre Reinforced Concrete (UHPFRC). *Construction and Building Material*s 37:874-882.

Hecker, S. S., M. G. Stout, K. P. Staudhammer, and J. L. Smith. 1982. Effects of strain state and strain rate on deformation-induced transformation in 304 stainless steel: Part I. Magnetic measurements and mechanical behavior. *Metallurgical Transactions A* 13(4):619-626.

Lin, Z., T. Kanda, and V. C. Li. 1999. On interface property characterization and performance of fiber-reinforced cementitious composites. *Concrete Science and Engineering* 1:173-184.

Mangonon, P. L., and G. Thomas. 1970. Structure and properties of thermal-mechanically treated 304 stainless steel. *Metallurgical Transactions* 1:1587-94.

Mumtaz, K., S. Takahashi, J. Echigoya, Y. Kamada, L. F. Zhang, H. Kikuchi, K. Ara, and M. Sato. 2004. Magnetic measurements of martensitic transformation in austenitic stainless steel after room temperature rolling. *Journal of Materials Scienc*e 39(1):85-97.

Murr, L. E., K. P. Staudhammer, and S. S. Hecker. 1982. Effects of strain state and strain rate on deformation-induced transformation in 304 stainless steel: Part II. Microstructural study. *Metallurgical and Materials Transactions A* 13(4):627-635.

Naaman, A. E., and H. Najm. 1991. Bond-slip mechanisms of steel fibers in concrete. *ACI Materials Journal* 88(2):135-145.

Naaman, A. E. 2003. Engineered steel fibers with optimal properties for reinforcement of cement composites. *Journal of Advanced Concrete Technology* 1(3):241-252.

Reinhart, W. D., and T. F. Thornhill III. 2010. *Ballistic penetration test results for Ductal and ultra-high performance concrete samples*. No. SAND2010-2222. Albuquerque, N.M.: Sandia National Laboratories.

Rivera-Soto, P., R. D. Moser, Z. B. McClelland, B. A. Williams, and S. L. Williams. 2016. Thermal processing and alloys selection to modify steel fiber performance in ultra-high performance concrete. *First International Interactive Symposium on UHPC, 18-20 July, Des Moines, Iowa*. Des Moines: Iowa State University.

Roth, J. M., S. T. Rushing, G. O. Flores, D. Sham, and J. W. Stevens. 2010. *Laboratory investigation of the characterization of Cor-Tuf flexural and splitting tensile properties*. ERDC/GSL-TR-10-46. Vicksburg, MS: U.S. Army Engineer Research and Development Center.

Ryu, S., S. T. Kang, J. J. Park, K. T. Koh, and S. W. Kim. 2011. Evaluation of fundamental UHPC properties according to the shape of steel fiber. *Key Engineering Materials* 452-453:717-720.

Scott, D. A., W. R. Long, R. D. Moser, B. H. Green, J. L. O'Daniel, and B. A. Williams. 2015. *Impact of steel fiber size and shape on the mechanical properties of ultra-high performance concrete*. ERDC/GSL TR-15-22. Vicksburg, MS: U.S. Army Engineer Research and Development Center.

Stout, M. G., and P. S. Follansbee. 1986. Strain rate sensitivity, strain hardening, and yield behavior of 304 L stainless steel. *Journal of Engineering Materials and Technology (Trans. ASME)* 108(4):344-353.

Talonen, J., H. Hänninen, P. Nenonen, and G. Pape. 2005. Effect of strain rate on the strain-induced γ→α′-martisite transformation and mechanical properties of austenitic stainless steels. *Metallurgical and Materials Transactions A* 36(2):421-432. doi.org/10.1007/s11661-005-0313-y.

Tang, F., G. Chen, R. K. Brow, J. S. Volz, and M. L. Koenigstein. 2012. Corrosion resistance and mechanism of steel rebar coated with three types of enamel. *Corrosion Science* 59:157-168.

Wang, X. H., S. Jacobsen, J. Y. He, Z. L. Zhang, S. F. Lee, and H. L. Lein. 2009. Application of nanoindentation testing to study of the interfacial transition zone in steel fiber reinforced mortar. *Cement and Concrete Research* 39(8):701-715.

Wille, K., and A. E. Naaman. 2012. Pullout behavior of high-strength steel fibers embedded in ultra-high-performance concrete. *ACI Materials Journal* 109(4):479-488.

Wille, K., and A. E. Naaman. 2013. Effect of ultra-high-performance concrete on pullout behavior of high-strength brass-coated straight steel fibers. *ACI Materials Journal* 110(4):451-462.

Williams, E. M., S. S. Graham, P. A. Reed, and T. S. Rushing. 2009. *Laboratory characterization of Cor-Tuf concrete with and without steel fibers*. ERDC/GSL TR-09-22. Vicksburg, MS: U.S. Army Engineer Research and Development Center.

Wu, Z., C. Shi, and K. H. Khayat. 2016. Influence of silica fume content on microstructure development and bond to steel fiber in ultra-high strength cement-based materials (UHSC). *Cement & Concrete Composites* 71:97-109.

Yan, D., S. Reis, X. Tao, G. Chen, R. K. Brow, and M. Koenigstein. 2012. Effect of chemically reactive enamel coating on bonding strength at steel/mortar interface. *Construction and Building Materials* 28(1):512-518.

Yan, D., H. Yin, C. Wu, Y. Li, J. Baird, and G. Chen. 2016. Blast response of full-size concrete walls with chemically reactive enamel (CRE)-coated steel reinforcement. *Journal of Zhejiang University Science A. (Applied Physics & Engineering)* 17(9):689-701. https://doi.org/10.1631/jzus.A1600480.

Appendix A: BEKAERT Steel Fiber Data Sheets

Dramix®

BEKAERT
better together

Data Sheet

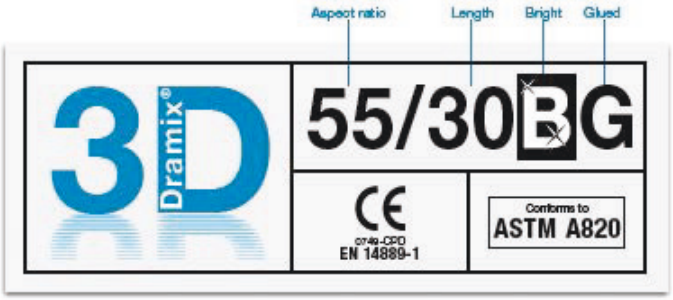

DRAMIX® 3D

Dramix® 3D is the reference in steel fibre reinforcement. Combining high performance, durability and ease-of-use, 3D provides you with a time-saving and cost-efficient solution for most common applications.

> original anchorage
> standard tensile strength

Dramix® 3D is a cost efficient solution for
> flooring
> tunnel applications
> precast
> residential applications

Bekaert supplies all of the support you need for your project. We help you determine the most suitable fibre types, calculate optimal dosages, select the right concrete quality. Contact your local support.

Go to www.bekaert.com/dosingdramix for our recommendations on handling, dosing and mixing.

Modifications reserved.
All details describe our products in general form only. For detailed information, product specifications available on request.

PERFORMANCE

Material properties

Tensile strength: $R_{m,nom}$: 1.345 N/mm²
Tolerances: ± 7,5% Avg
Young's Modulus: ± 200.000 N/mm²

Geometry

Fibre family 3D

Length (l) 30 mm

Diameter (d) 0,55 mm

Aspect ratio (l/d) 55

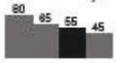

Fibre network

13,4 km per m³ (for 25 kg/m³)
17.054 fibres/kg

Dramix® range

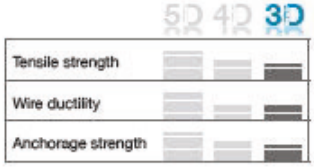

PRODUCT CERTIFICATES

CE 0749-CPD EN 14889-1
Conforms to ASTM A820

Dramix® is certified for structural use according to EN 14889-1 (system '1'). Detailed information is available on request.

SYSTEM CERTIFICATES

All Dramix® plants are ISO 9001 and ISO 14001 certified.

PACKAGING

BAGS 20 kg

BIG BAG 800-1100 kg

STORAGE

Dramix®

BEKAERT
better together

Data Sheet

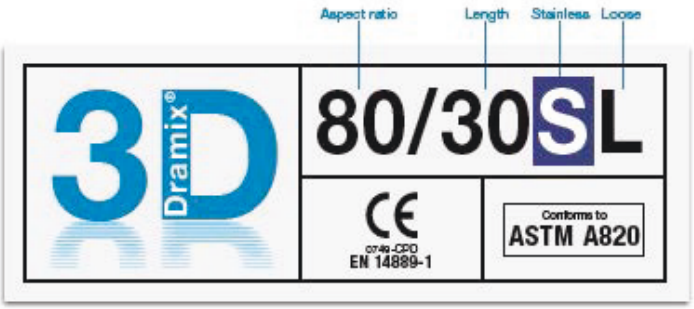

DRAMIX® 3D

Dramix® 3D is the reference in steel fibre reinforcement. Combining high performance, durability and ease-of-use, 3D provides you with a time-saving and cost-efficient solution for most common applications.

> original anchorage
> standard tensile strength

Dramix® 3D is a cost efficient solution for
> flooring
> tunnel applications
> precast
> residential applications

Bekaert supplies all of the support you need for your project. We help you determine the most suitable fibre types, calculate optimal dosages, select the right concrete quality. Contact your local support.

Go to www.bekaert.com/dosingdramix for our recommendations on handling, dosing and mixing.

Modifications reserved.
All details describe our products in general form only. For detailed information, product specifications available on request.

PERFORMANCE

Material properties

Tensile strength: $R_{m,min}$: 2.000 N/mm²
Tolerances: ± 7,5% Avg
Young's Modulus: ± 200.000 N/mm²

Geometry

Fibre family 3D

Length (l) 30 mm

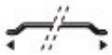

Diameter (d) 0,38 mm

Aspect ratio (l/d) 80

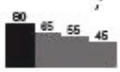

Fibre network

22,4 km per m³ (for 20 kg/m³)
35.388 fibres/kg

Dramix® range

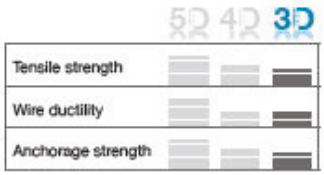

PRODUCT CERTIFICATES

CE 0749-CPD EN 14889-1 — Conforms to ASTM A820

Dramix® is certified for structural use according to EN 14889-1 (system '1'). Detailed information is available on request.

SYSTEM CERTIFICATES

All Dramix® plants are ISO 9001 and ISO 14001 certified.

PACKAGING

BOXES 20 kg

STORAGE

Appendix B: Dynamic Impact Pictures

B.1 CS 1 inch

Figure B16. Carbon steel dynamic impact 1-in. thickness.

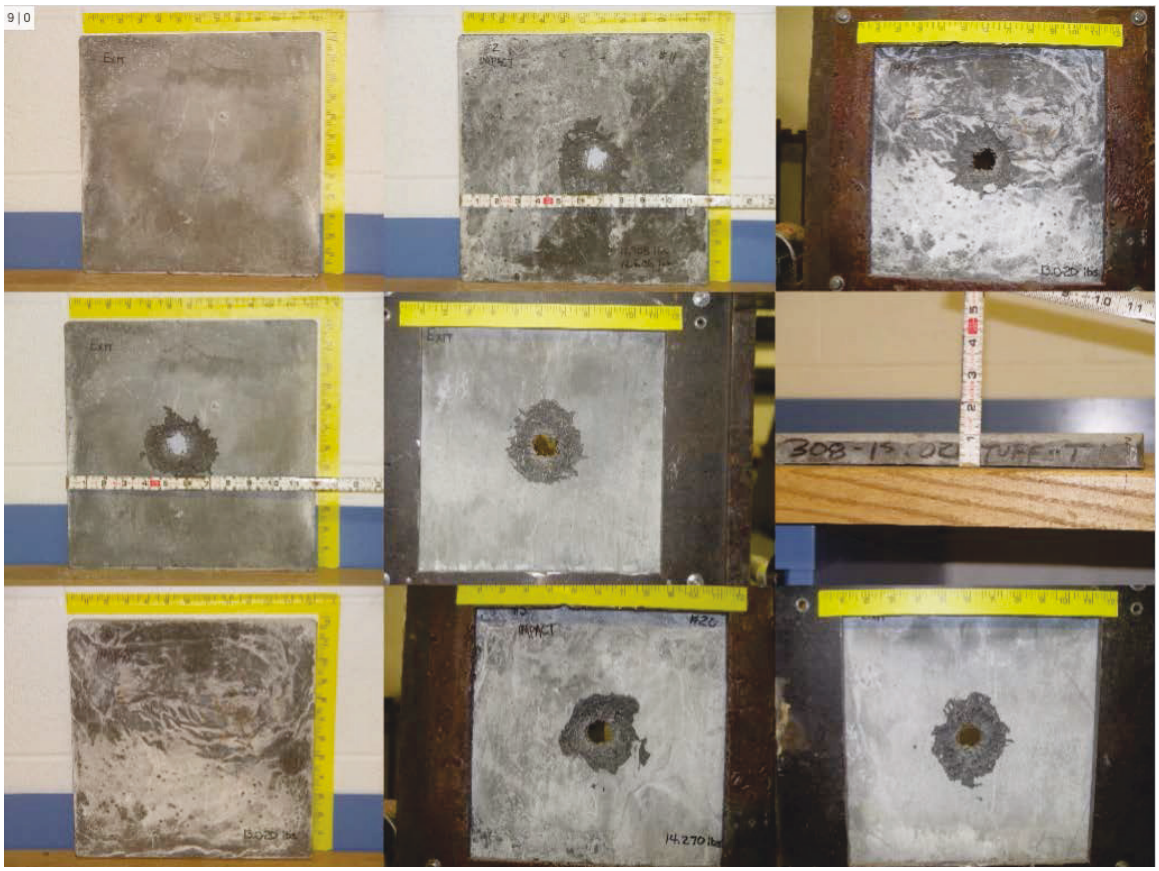

B.2 SS 1 inch

Figure B17. Stainless steel dynamic impact 1-in. thickness.

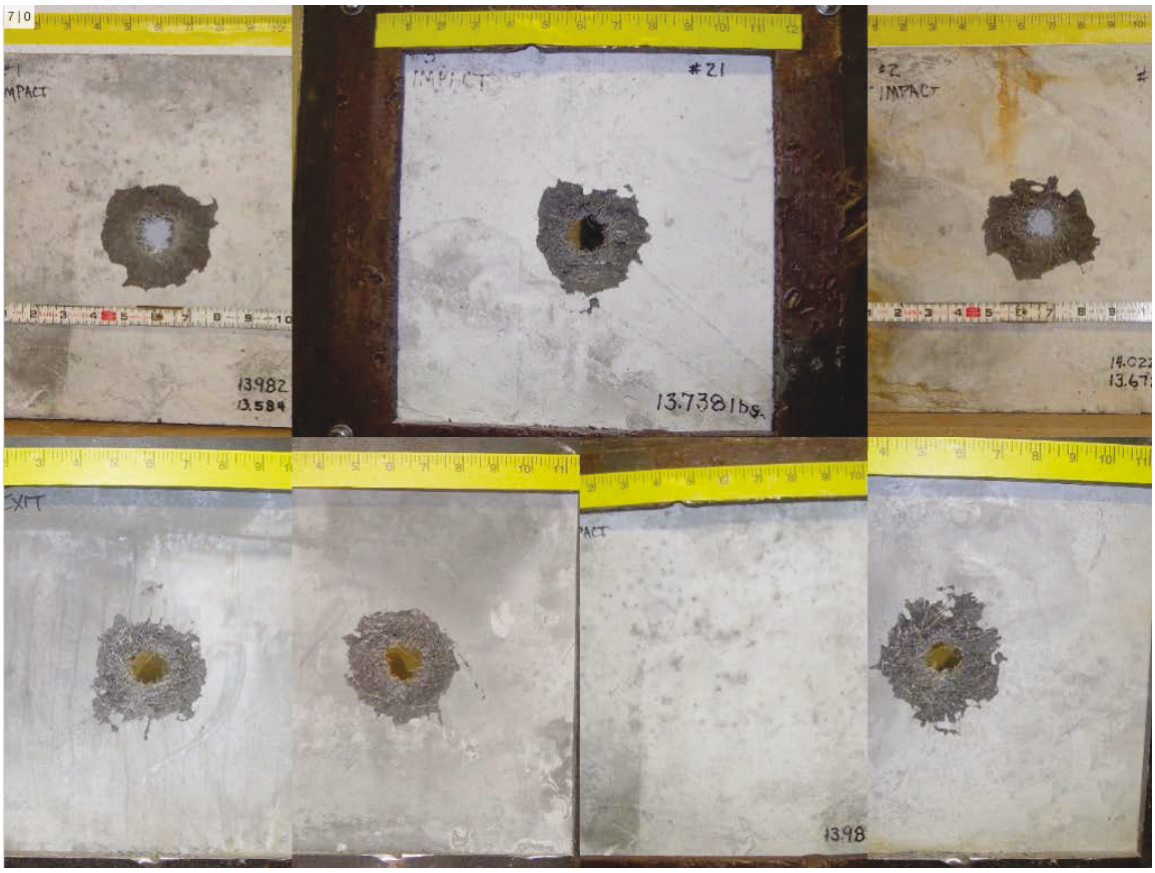

B.3 AC 1 inch

Figure B18. Annealed carbon steel dynamic impact 1-in. thickness.

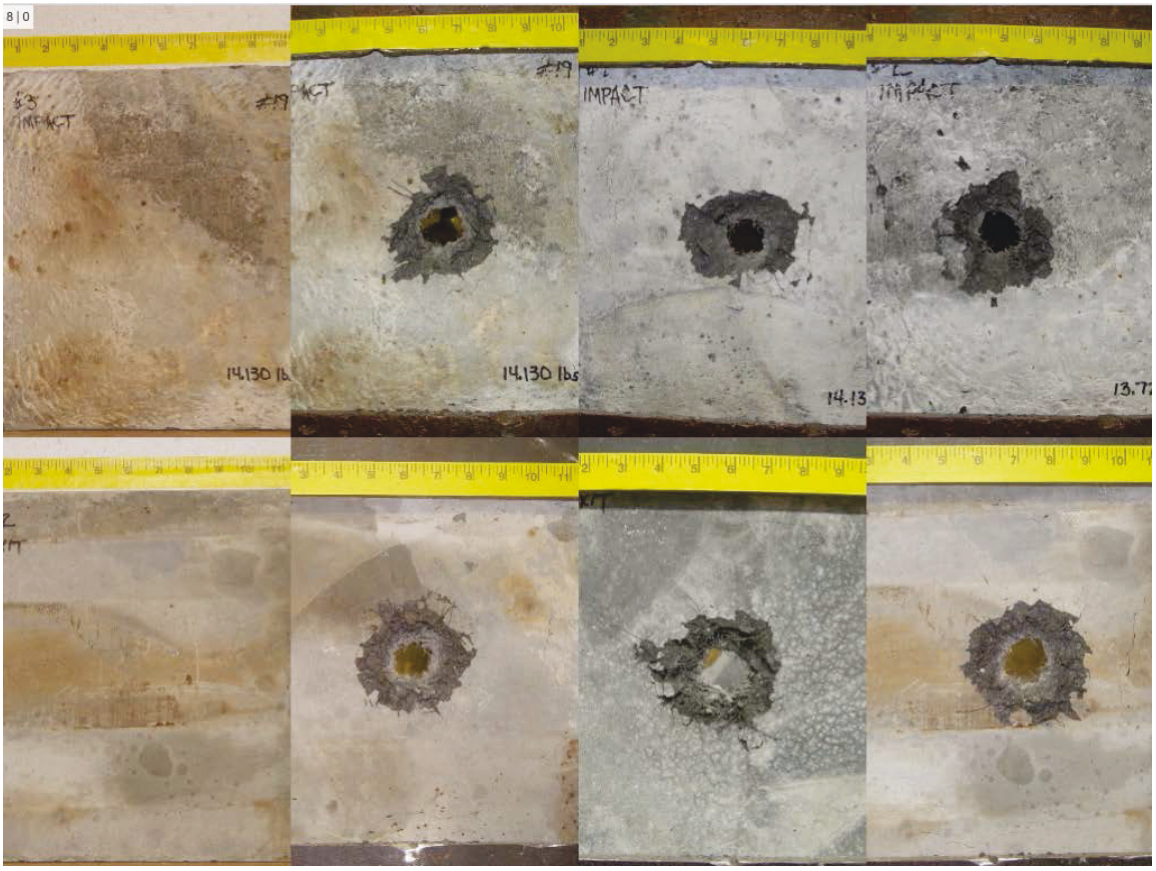

B.4 CS 2 inch

Figure B19. Carbon steel dynamic impact 2-in. thickness.

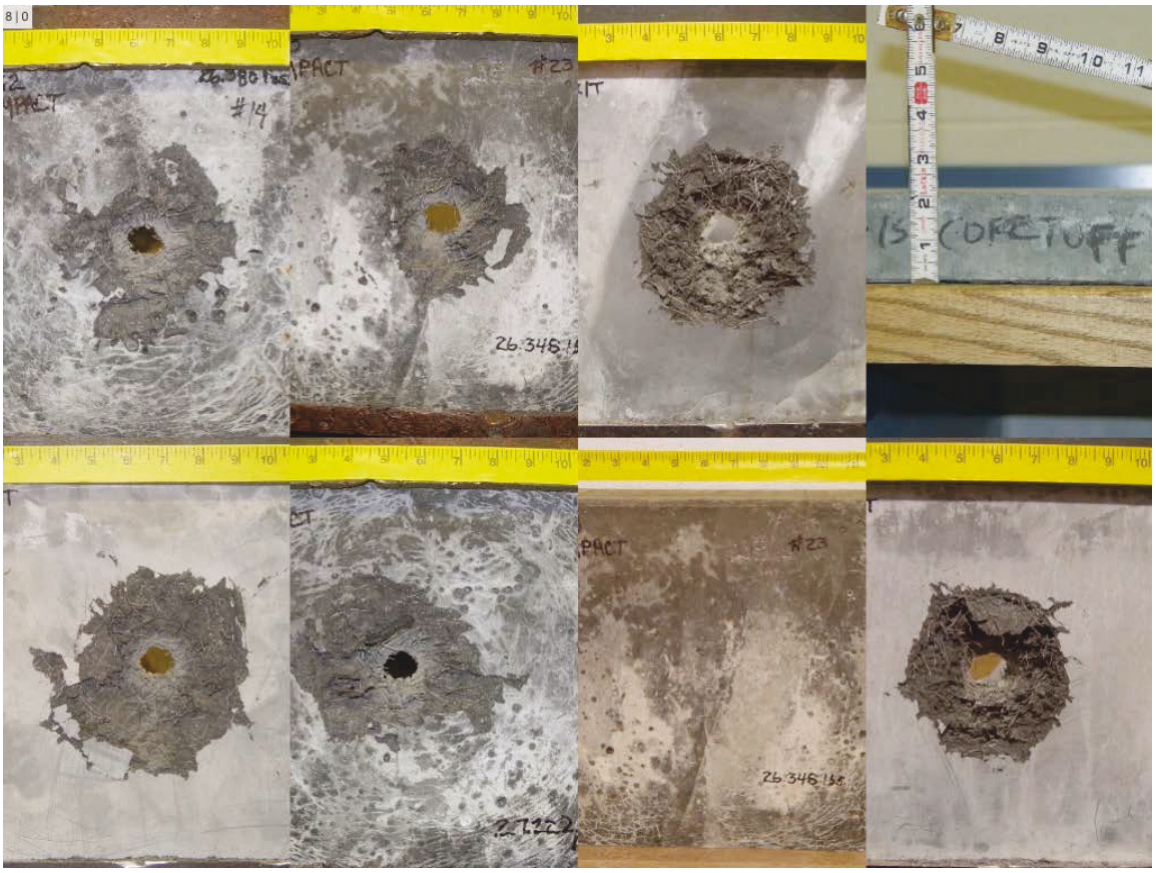

B.5 SS 2 inch

Figure B20. Stainless steel dynamic impact 2-in. thickness.

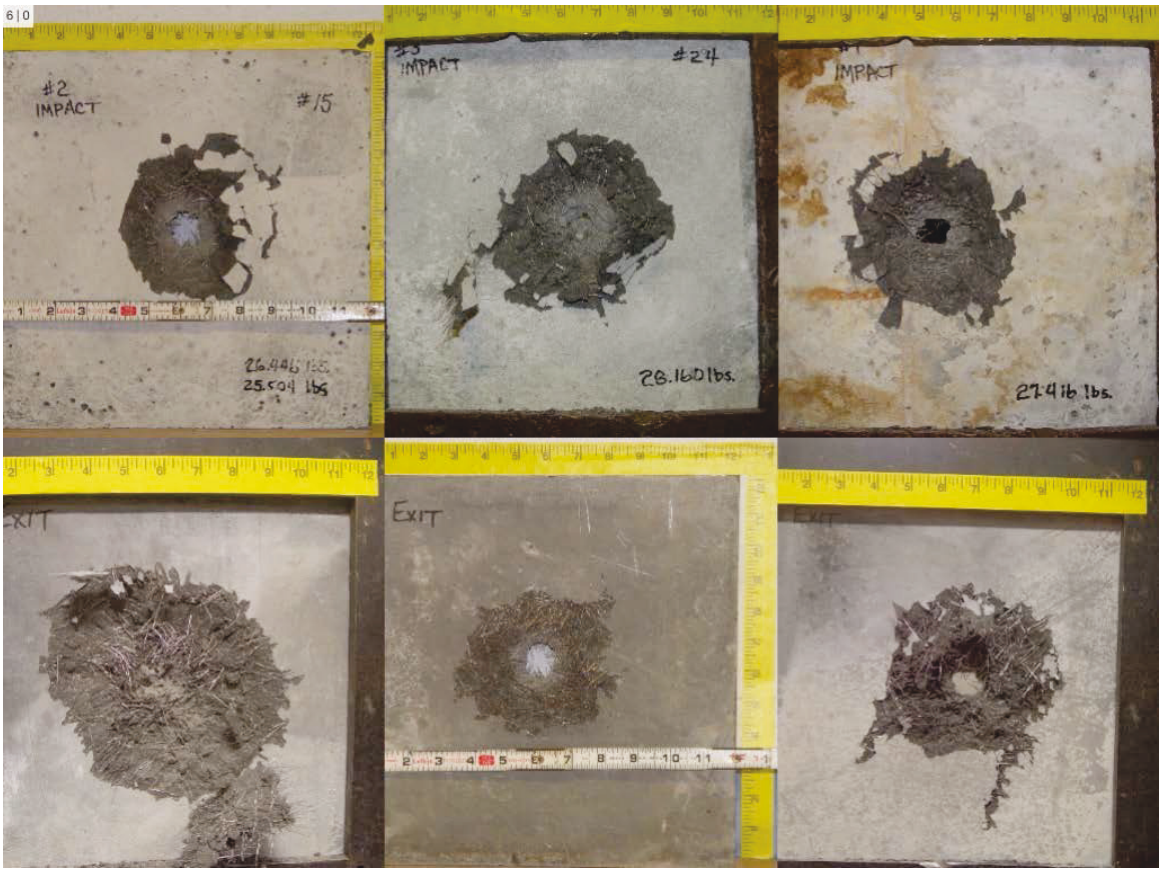

B.6 AC 2 inch

Figure B21. Annealed carbon steel dynamic impact 2-in. thickness.

B.7 CS 2.5 inch

Figure B22. Carbon steel dynamic impact 2.5-in. thickness.

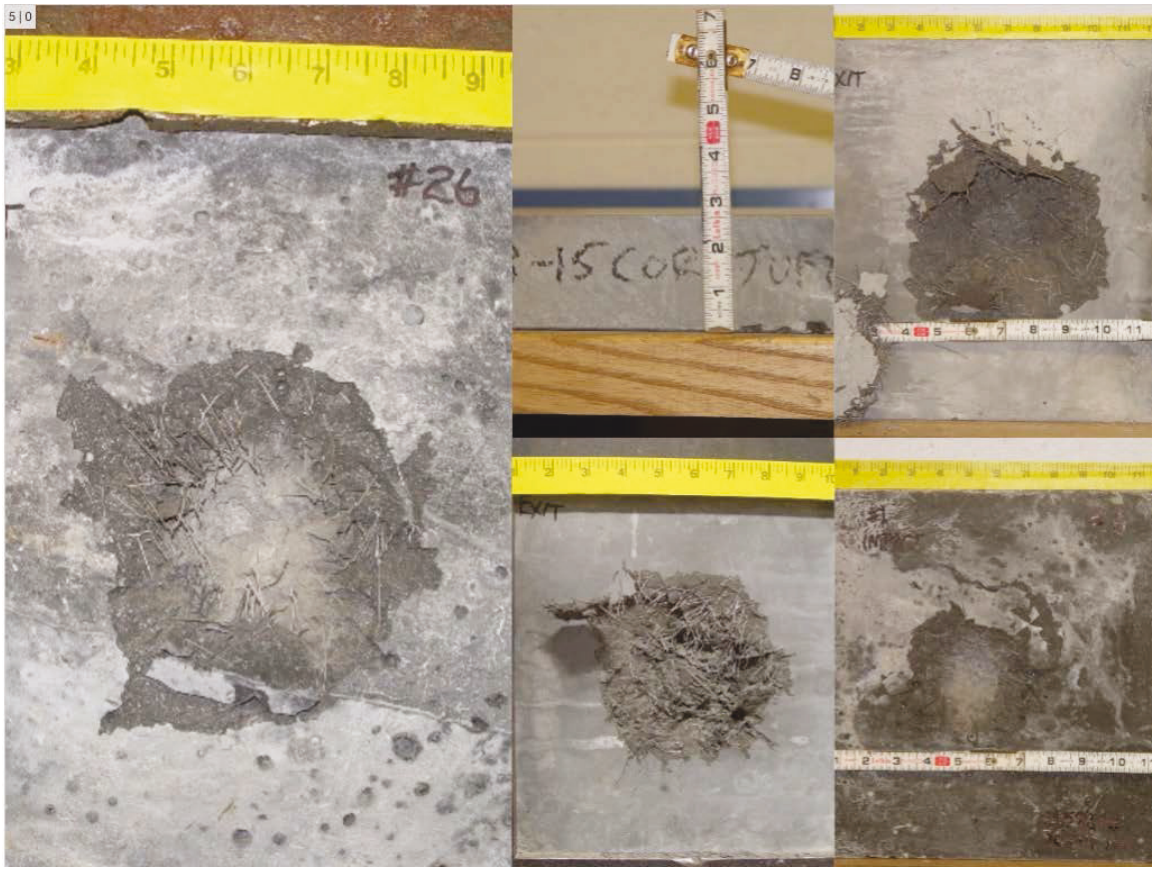

B.8 SS 2.5 inch

Figure B23. Stainless steel dynamic impact 2.5-in. thickness.

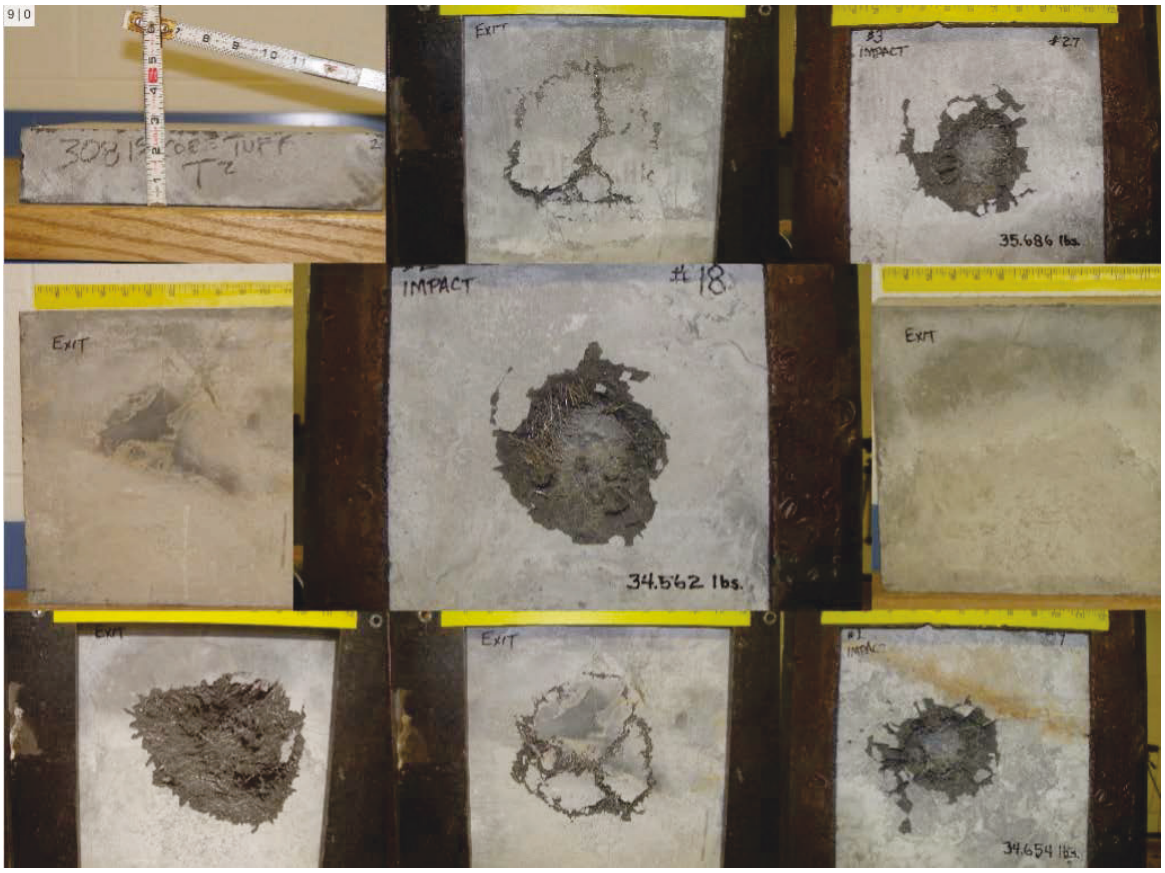

B.9 AC 2.5 inch

Figure B24. Annealed carbon steel dynamic impact 2.5-in. thickness.

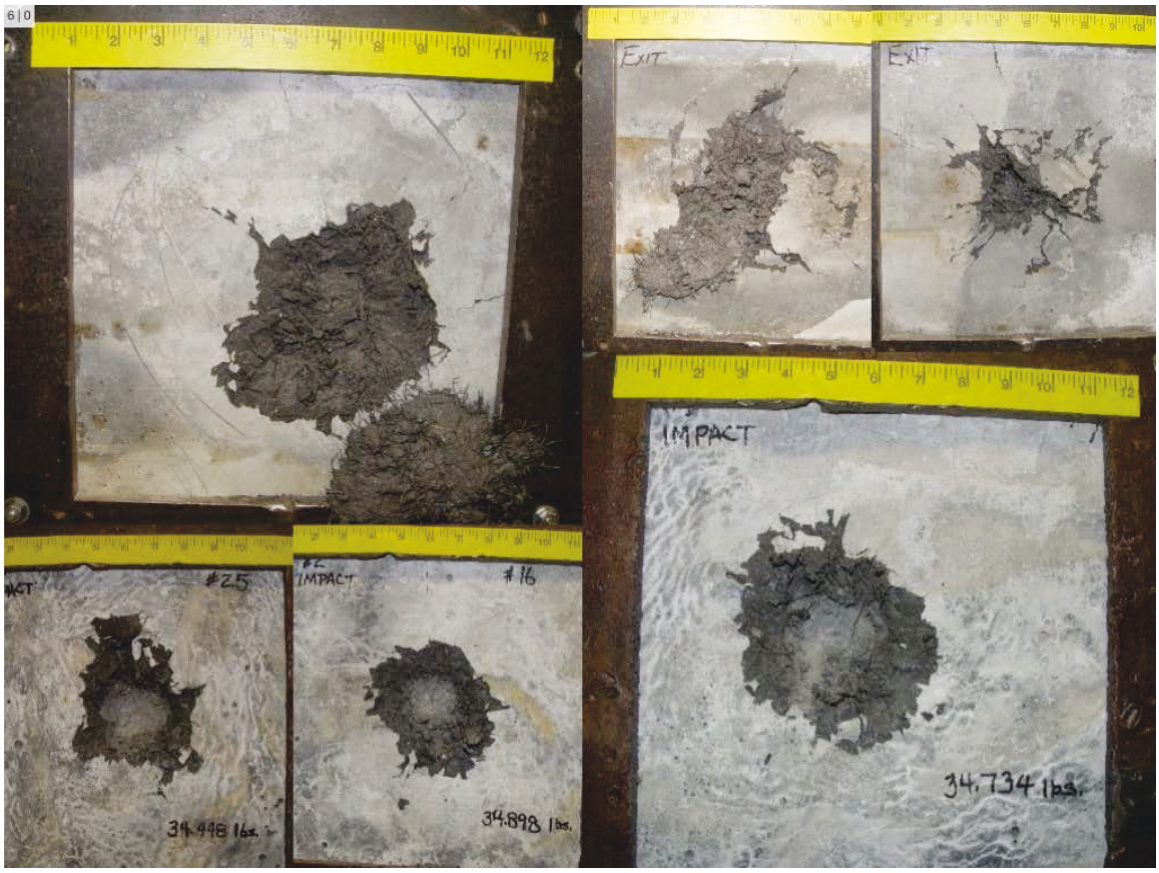

REPORT DOCUMENTATION PAGE

Form Approved
OMB No. 0704-0188

1. REPORT DATE *(DD-MM-YYYY)*	2. REPORT TYPE	3. DATES COVERED *(From - To)*
March 2019	Final	

4. TITLE AND SUBTITLE

Introducing Additional Energy Dissipation Mechanisms in Steel Fiber Reinforcement for Ultra-High Performance Concrete

5a. CONTRACT NUMBER

5b. GRANT NUMBER

5c. PROGRAM ELEMENT NUMBER

6. AUTHOR(S)

Dylan A. Scott, Robert D. Moser, Zackery B. McClelland, Sarah L. Williams, Brett A. Williams, Wendy R. Long, Brian H. Green, Kirk E. Walker, Christopher N. Downey, Alexander J. Tillotson

5d. PROJECT NUMBER
F7CJL4

5e. TASK NUMBER

5f. WORK UNIT NUMBER

7. PERFORMING ORGANIZATION NAME(S) AND ADDRESS(ES)

Geotechnical and Structures Laboratory
U.S. Army Engineer Research and Development Center
3909 Halls Ferry Road
Vicksburg, MS 39180-6199

8. PERFORMING ORGANIZATION REPORT NUMBER

ERDC/GSL TR-19-9

9. SPONSORING / MONITORING AGENCY NAME(S) AND ADDRESS(ES)

U.S. Army Corps of Engineers
Washington, DC 20314-1000

10. SPONSOR/MONITOR'S ACRONYM(S)

USACE

11. SPONSOR/MONITOR'S REPORT NUMBER(S)

12. DISTRIBUTION / AVAILABILITY STATEMENT

Approved for public release; distribution is unlimited.

13. SUPPLEMENTARY NOTES

14. ABSTRACT

By adding annealed plain carbon steel fibers and stainless steel fibers into Ultra-High Performance Concrete (UHPC), researchers have increased UHPC's toughness through optimized thermal processing and alloy selection of steel fiber reinforcements. Currently, steel fiber reinforcements used in UHPCs are extremely brittle and have limited energy dissipation mainly through debonding due to matrix crumbling with some pullout. Implementing optimized heat treatments and selecting proper alternative alloys can drastically improve the post-yield carrying capacity of UHPCs for static and dynamic applications through plastic deformations, phase transformations, and fiber pullout. By using a phase transformable stainless steel, the ultimate flexural strength increased from 32.0 MPa to 42.5 MPa (33 percent) and decreased the post-impact or residual projectile velocity measurements an average of 31.5 m/s for 2.54-cm- and 5.08-cm-thick dynamic impact panels.

15. SUBJECT TERMS

UHPC
Cor-Tuf
High strength concrete
Concrete
Fiber Reinforcement
Steel
Steel-Heat treatment
Penetration
Mechanical Properties
Fibers
Fiber-reinforced concrete

16. SECURITY CLASSIFICATION OF:			17. LIMITATION OF ABSTRACT	18. NUMBER OF PAGES	19a. NAME OF RESPONSIBLE PERSON
a. REPORT	b. ABSTRACT	c. THIS PAGE			19b. TELEPHONE NUMBER *(include area code)*
Unclassified	Unclassified	Unclassified		61	